

AD \_\_\_\_\_

GRANT NUMBER DAMD17-96-1-6093

TITLE: An Overcomplete Enhancement of Digital Mammograms

PRINCIPAL INVESTIGATOR: Dr. Fred Taylor  
Iztok Koren, Ph.D.

CONTRACTING ORGANIZATION: University of Florida  
Gainesville, FL 32611

REPORT DATE: August 1997

TYPE OF REPORT: Annual

PREPARED FOR: Commander  
U.S. Army Medical Research and Materiel Command  
Fort Detrick, Frederick, Maryland 21702-5012

DISTRIBUTION STATEMENT: Approved for public release;  
distribution unlimited

The views, opinions and/or findings contained in this report are those of the author(s) and should not be construed as an official Department of the Army position, policy or decision unless so designated by other documentation.

DTIC QUALITY INSPECTED 3

19980114 109

# REPORT DOCUMENTATION PAGE

Form Approved  
OMB No. 0704-0188

Public reporting burden for this collection of information is estimated to average 1 hour per response, including the time for reviewing instructions, searching existing data sources, gathering and maintaining the data needed, and completing and reviewing the collection of information. Send comments regarding this burden estimate or any other aspect of this collection of information, including suggestions for reducing this burden, to Washington Headquarters Services, Directorate for Information Operations and Reports, 1215 Jefferson Davis Highway, Suite 1204, Arlington, VA 22202-4302, and to the Office of Management and Budget, Paperwork Reduction Project (0704-0188), Washington, DC 20503.

<b>1. AGENCY USE ONLY (Leave blank)</b>		<b>2. REPORT DATE</b> August 1997	<b>3. REPORT TYPE AND DATES COVERED</b> Annual (1 Aug 96 - 31 Jul 97)	
<b>4. TITLE AND SUBTITLE</b> An Overcomplete Enhancement of Digital Mammograms			<b>5. FUNDING NUMBERS</b> DAMD17-96-1-6093	
<b>6. AUTHOR(S)</b> Dr. Fred Taylor Istok Koren, Ph.D.				
<b>7. PERFORMING ORGANIZATION NAME(S) AND ADDRESS(ES)</b> University of Florida Gainesvill, FL 32611			<b>8. PERFORMING ORGANIZATION REPORT NUMBER</b>	
<b>9. SPONSORING/MONITORING AGENCY NAME(S) AND ADDRESS(ES)</b> Commander U.S. Army Medical Research and Materiel Command Fort Detrick, Frederick, Maryland 21702-5012			<b>10. SPONSORING/MONITORING AGENCY REPORT NUMBER</b>	
<b>11. SUPPLEMENTARY NOTES</b>				
<b>12a. DISTRIBUTION / AVAILABILITY STATEMENT</b>  Approved for public release; distribution unlimited			<b>12b. DISTRIBUTION CODE</b>	
<b>13. ABSTRACT (Maximum 200)</b>  In this report, we describe recent progress in the development of methodology for providing radiologists with a better viewing environment to facilitate the interpretation of mammograms. Our research has been directed towards local processing of images for enhancement of features of diagnostic importance in mammography, and towards development of image fusion methods for blending of enhanced features for an improved visualization of mammograms.  We report on the construction of a redundant steerable wavelet transform for multiscale analysis along distinct orientations. We have addressed both elimination of undesirable artifacts commonly associated with wavelet transforms, and efficient implementation of the transform. From qualitative and quantitative comparisons with competitive transforms for fusion of features in mammography, we conclude that the transform is well suited for enhancement of mammograms. By improving the visualization of breast pathology, we can improve chances of early detection while requiring less time to evaluate mammograms for most patients.				
<b>14. SUBJECT TERMS</b> Breast Cancer			<b>15. NUMBER OF PAGES</b> 72	
			<b>16. PRICE CODE</b>	
<b>17. SECURITY CLASSIFICATION OF REPORT</b> Unclassified	<b>18. SECURITY CLASSIFICATION OF THIS PAGE</b> Unclassified	<b>19. SECURITY CLASSIFICATION OF ABSTRACT</b> Unclassified	<b>20. LIMITATION OF ABSTRACT</b> Unlimited	

## FOREWORD

Opinions, interpretations, conclusions and recommendations are those of the author and are not necessarily endorsed by the U.S. Army.

\_\_\_\_ Where copyrighted material is quoted, permission has been obtained to use such material.

\_\_\_\_ Where material from documents designated for limited distribution is quoted, permission has been obtained to use the material.

AA Citations of commercial organizations and trade names in this report do not constitute an official Department of Army endorsement or approval of the products or services of these organizations.


\_\_\_\_ In conducting research using animals, the investigator(s) adhered to the "Guide for the Care and Use of Laboratory Animals," prepared by the Committee on Care and Use of Laboratory Animals of the Institute of Laboratory Resources, National Research Council (NIH Publication No. 86-23, Revised 1985).

\_\_\_\_ For the protection of human subjects, the investigator(s) adhered to policies of applicable Federal Law 45 CFR 46.

\_\_\_\_ In conducting research utilizing recombinant DNA technology, the investigator(s) adhered to current guidelines promulgated by the National Institutes of Health.

\_\_\_\_ In the conduct of research utilizing recombinant DNA, the investigator(s) adhered to the NIH Guidelines for Research Involving Recombinant DNA Molecules.

\_\_\_\_ In the conduct of research involving hazardous organisms, the investigator(s) adhered to the CDC-NIH Guide for Biosafety in Microbiological and Biomedical Laboratories.

  
\_\_\_\_  
PI - Signature

9-3-97  
\_\_\_\_  
Date

# Table of Contents

<b>1</b>	<b>Introduction</b>	<b>7</b>
1.1	Overview of Contents . . . . .	8
1.2	Publications . . . . .	9
1.3	Notation . . . . .	10
<b>2</b>	<b>Body</b>	<b>12</b>
2.1	Signal Processing Using Central B-Splines . . . . .	12
2.1.1	Central B-Splines: Definition and Properties . . . . .	12
2.1.2	B-Spline Signal Interpolations . . . . .	14
2.1.3	B-Spline Signal Approximations . . . . .	16
2.2	Steerable Dyadic Transforms . . . . .	19
2.2.1	Shortcomings of Traditional Methods of Wavelet Analysis . . . . .	20
2.2.2	1-D Discrete Dyadic Wavelet Transform Revisited . . . . .	22
2.2.3	Remarks . . . . .	31
2.2.4	2-D Discrete Dyadic Wavelet Transform Revisited . . . . .	32
2.2.5	Steerable Functions . . . . .	37
2.2.6	Steerable Dyadic Wavelet Transform . . . . .	39
2.2.7	Multiscale Spline Derivative-Based Transform . . . . .	43
2.2.8	Finite Impulse Response Filters . . . . .	47
2.2.9	Infinite Impulse Response Filters . . . . .	54
2.3	Image Fusion . . . . .	56
2.3.1	Gradient Pyramid . . . . .	57
2.3.2	Discrete Wavelet Transform . . . . .	58
2.3.3	Comparison of Transforms . . . . .	59
<b>3</b>	<b>Conclusions</b>	<b>67</b>
	<b>References</b>	<b>68</b>

## List of Tables

1	Transfer functions of direct B-spline filters for orders from 0 to 9. . . . .	15
2	Impulse responses $h(n)$ , $g(n)$ , $l(n)$ , and $k(n)$ for $p=0$ and $d \in \{1, 2, 3\}$ . . . .	29
3	Impulse responses $h(n)$ , $g(n)$ , $l(n)$ , and $k(n)$ for $p=1$ and $d \in \{1, 2, 3\}$ . . . .	29
4	Impulse responses $h(n)$ , $g(n)$ , $l(n)$ , and $k(n)$ for $p=2$ and $d \in \{1, 2, 3\}$ . . . .	31
5	Impulse responses $t_1(n)$ for $p \in \{0, 1, 2\}$ . . . . .	34
6	Performance of fusion algorithms based on four different transforms. . . . .	61

## List of Figures

1	Spline functions $\beta_p(x)$ and $\eta_p(x)$ for $p \in \{0, 1, 2, 3, 4\}$ . . . . .	13
2	Fourier transforms $\hat{\beta}_p(\omega)$ and $\hat{\eta}_p(\omega)$ for $p \in \{0, 1, 2, 3, 4\}$ . . . . .	17
3	Splines $\overset{\circ}{\beta}_p(x)$ and $\overset{\circ}{\beta}_p(\omega)$ for $p \in \{0, 1, 2, 3, 4\}$ . . . . .	18
4	Discrete wavelet transform of two signals translated to each other. . . . .	21
5	Discrete wavelet transform and “algorithme à trous.” . . . .	22
6	Filter bank implementation of a 1-D discrete dyadic wavelet transform. . . .	26
7	Comparison of two discrete implementations using $\text{sinc}(x)$ as an input. . . .	27
8	Wavelets $\psi(x) = \frac{d^d \beta_{p+d}(x)}{dx^d}$ for $p \in \{0, 1, 2\}$ and $d \in \{1, 2, 3\}$ . . . . .	30
9	Filter bank implementation of a 2-D discrete dyadic wavelet transform. . . .	36
10	Filter coefficients for the second derivative steerable dyadic wavelet transform. .	41
11	Filter coefficients for the fourth derivative steerable dyadic wavelet transform. .	42
12	Filter bank implementation of a spline derivative-based transform. . . . .	49
13	Phantom used for comparisons of different transforms for image fusion. . . .	60
14	Image fusion of phantoms shifted by one sample. . . . .	62
15	Image fusion of phantoms shifted by five samples. . . . .	63
16	Blurred mammograms for evaluation of fusion algorithms. . . . .	64
17	Zooming in on the region of interest in the fused images. . . . .	66

# 1 Introduction

Breast cancer is the most frequently diagnosed malignancy among women in the United States [1]. In 1996 the American Cancer Society estimates that 184,300 women will be newly diagnosed with breast cancer and that 44,300 will die from the disease [1]. Breast cancer accounts for 31% of all cancers detected and 17% of all cancer deaths, and ranks as the second leading cause of death from cancer among women in the United States [1]. Five year survival rates are generally very high (93%) for breast cancer staged as being localized, falling to 72% for regional disease and only 18% for distant disease [2]. The early detection of breast cancer is clearly a key ingredient of any strategy designed to reduce breast cancer mortality.

Mammography's role is the early detection of breast cancer. Although more accurate than any other modality, existing techniques for mammography only find 80 to 90% of the breast cancers. Moreover, in 7 to 10% of cases, the cancer will not be visible on the mammogram. It has been suggested that mammograms as normally viewed, display only about 3% of the total information detected. Perception is a problem particularly for patients with dense fibroglandular patterns. The importance of diagnosis of breast cancer at an early stage is critical to patient survival. The general inability to detect small tumors and other salient features within mammograms motivates our investigation.

The goal of this project is to develop a diagnostic tool for radiologists that will refine the perception of mammographic features (including lesions, masses and calcifications) and improve the accuracy of diagnosis. Our research efforts are geared towards improving the local mammographic viewing environment by selectively processing mammograms along different orientations, and towards providing a better global mammographic viewing environment by fusing together locally processed sections of images. By improving the visualization of breast pathology we can increase the chances of early detection of breast cancers (improve quality) while requiring less time to evaluate mammograms for most patients (lower costs).

A major reason for poor visualization of small malignant masses is the subtle difference in x-ray attenuation between normal glandular tissues and malignant disease [3]. This fact makes the detection of small malignancies problematical, especially in younger women who have denser breast tissue. Although calcifications have high inherent attenuation properties, their small size also results in a low subject contrast [4]. As a result, the visibility of small tumors, and any associated microcalcifications, will always be a problem in mammography as it is currently performed using analog film.

We are investigating a methodology for accomplishing mammographic feature analysis

through multiscale representations. Wide variety of feature sizes and shapes in mammograms makes single-scale processing methods ineffective. In [5], it was shown that, in the context of mammography, multiscale image processing algorithms can outperform traditional contrast enhancement methods such as histogram equalization and unsharp masking. As reported in [6], an improvement in feature visualization was noted for mammograms processed using multiscale wavelet processing techniques. Furthermore, in [7], it was demonstrated that unsharp masking with a Gaussian lowpass filter can be formulated as a special case of contrast enhancement via a discrete dyadic wavelet transform. Here, we pay special attention to two-dimensional extensions of a discrete dyadic wavelet transform that enable efficient directional processing of mammographic images, and then examine the usefulness of the derived transform for image fusion in mammography.

In the sections that follow, we briefly overview the contents of the report, list publications, and explain notation used in the report.

## 1.1 Overview of Contents

Discrete dyadic wavelet transform has been successfully applied to processing of mammographic images [8, 5, 7, 9, 10]. Since the transform uses wavelets that are derivatives of central B-spline functions, we begin Section 2 with a review of central B-splines' properties and algorithms.

Extensions of the discrete dyadic wavelet transform are presented in Section 2.2. Since the transform is of paramount importance in our methodology for improving the imaging performance of mammography, this section represents the largest portion of the report. First, some of the shortcomings of orthogonal and biorthogonal wavelet analyses are presented in Section 2.2.1. Lack of translation and rotation invariance of these transforms motivates the use of redundant representations. Next, Section 2.2.2, examines a dyadic wavelet transform in one dimension. We present extensions of the discrete dyadic wavelet transform to higher order derivatives and to even order spline functions. To compute a discrete transform from a continuous one, the discrete computation must be properly initialized. We devise a new initialization procedure that is shown to be more accurate than the one suggested by Mallat and Zhong [11]. After the derivation of the transform, we point out relevant connections to scale-space filtering and reconstruction from edges in Section 2.2.3. Section 2.2.4 then presents a direct extension of the one-dimensional transform to two dimensions. In case of the first derivative of a Gaussian, a rotation-invariant transform can be obtained by a tensor product extension of the one-dimensional transform to two dimensions. Anisotropies introduced by the two-dimensional second derivative discrete



dyadic wavelet transform may be avoided by combining derivatives into an isotropic operator, such as Laplacian of Gaussian [7, 10]. Such an operator, however, cannot perform orientation analysis (due to its isotropic nature). To lay grounds for effective directional operators, the concept of steerability is reviewed in Section 2.2.5. Steerable dyadic wavelet transform is constructed in Section 2.2.6, and its  $x$ - $y$  separable analog in Section 2.2.7. These transforms, in addition to being translation-invariant, enable rotation-invariant processing for derivatives of orders higher than two as well. Given that the developed transforms are highly redundant, an efficient implementation is extremely advantageous. This issue is addressed in Sections 2.2.8 and 2.2.9. When filtering of a signal is performed by circular convolution, boundary effects may result. A standard way of dealing with this problem is by mirror-extending the input signal to the filter. We build on ideas presented in [12], and combine such an extension with symmetry/antisymmetry of the filters, to achieve savings in both computation time and memory.

Section 2.3 deals with image fusion. First, two popular transforms for image fusion applications, the gradient pyramid and orthogonal/biorthogonal wavelet transform, are briefly presented in Sections 2.3.1 and 2.3.2. Comparison of the two transforms with steerable dyadic wavelet transform using subjective and objective criteria is presented in Section 2.3.3. Steerable dyadic wavelet transform did not introduce artifacts common for the orthogonal and biorthogonal wavelet transforms, while outperforming the gradient pyramid in terms of sharpness and mathematically defined error criteria.

## 1.2 Publications

Below, we provide the list of publications accomplished during the first year of the project.

- [1] I. Koren, A. Laine, and F. Taylor, "An overcomplete enhancement of digital mammograms," *Era of Hope, A Multidisciplinary Reporting of DoD Progress*, Washington, D.C., Oct.–Nov. 1997.
- [2] I. Koren and A. Laine, "A discrete dyadic wavelet transform for multidimensional feature analysis," in *Time-Frequency and Wavelets in Biomedical Signal Engineering*, M. Akay, Ed., IEEE Press, New York, NY, 1997, pp. 425–449.
- [3] S. Schuler, I. Koren, M. Shim, A. Laine, B. Steinbach, and W. Huda, "An interactive tutorial for contrast enhancement of digital mammograms via multiscale representations on the Web," *RSNA EJ*, 1997.
- [4] A. F. Laine, I. Koren, S. Schuler, W. Huda, and B. G. Steinbach, "Contrast enhancement of mammographic features via multiscale analysis," *RSNA 82nd Scientific*

*Assembly and Annual Meeting*, Chicago, IL, 1996.

### 1.3 Notation

We use symbols  $\mathbf{N}$ ,  $\mathbf{Z}$ , and  $\mathbf{R}$  for the sets of naturals, integers, and reals, respectively.  $L^2(\mathbf{R})$  and  $L^2(\mathbf{R}^2)$  denote the Hilbert spaces of measurable, square-integrable functions  $f(x)$  and  $f(x, y)$ , respectively.

The inner product of two functions  $f(x) \in L^2(\mathbf{R})$  and  $g(x) \in L^2(\mathbf{R})$  is given by

$$\langle f(x), g(x) \rangle = \int_{-\infty}^{\infty} f(x) g(x) dx.$$

The norm of a function  $f(x) \in L^2(\mathbf{R})$  is defined as

$$\|f\| = \sqrt{\int_{-\infty}^{\infty} |f(x)|^2 dx}.$$

The convolution of functions  $f(x) \in L^2(\mathbf{R})$  and  $g(x) \in L^2(\mathbf{R})$  is computed as

$$f * g(x) = \int_{-\infty}^{\infty} f(t) g(x - t) dt,$$

and the convolution of two functions  $f(x, y) \in L^2(\mathbf{R}^2)$  and  $g(x, y) \in L^2(\mathbf{R}^2)$  equals

$$f * g(x, y) = \int_{-\infty}^{\infty} \int_{-\infty}^{\infty} f(t_x, t_y) g(x - t_x, y - t_y) dt_x dt_y.$$

The Fourier transform of a function  $f(x) \in L^2(\mathbf{R})$  is defined as

$$\hat{f}(\omega) = \int_{-\infty}^{\infty} f(x) e^{-j\omega x} dx,$$

and the Fourier transform of a function  $f(x, y) \in L^2(\mathbf{R}^2)$  is equal to

$$\hat{f}(\omega_x, \omega_y) = \int_{-\infty}^{\infty} \int_{-\infty}^{\infty} f(x, y) e^{-j(\omega_x x + \omega_y y)} dx dy.$$

$l^2(\mathbf{Z})$  and  $l^2(\mathbf{Z}^2)$  stand for the spaces of square-summable discrete signals  $f(n)$  and  $f(n_x, n_y)$ , respectively.

The  $z$ -transform of a discrete signal  $f(n) \in l^2(\mathbf{Z})$  is defined as

$$F(z) = \sum_{n=-\infty}^{\infty} f(n) z^{-n}.$$

The convolution of discrete signals  $f(n) \in l^2(\mathbf{Z})$  and  $g(n) \in l^2(\mathbf{Z})$  is equal to

$$f * g(n) = \sum_{m=-\infty}^{\infty} f(m) g(n - m),$$

and the convolution of discrete signals  $f(n_x, n_y) \in l^2(\mathbf{Z}^2)$  and  $g(n_x, n_y) \in l^2(\mathbf{Z}^2)$  is given by

$$f * g(n_x, n_y) = \sum_{m_x=-\infty}^{\infty} \sum_{m_y=-\infty}^{\infty} f(m_x, m_y) g(n_x - m_x, n_y - m_y).$$

The Fourier transform of a discrete signal  $f(n) \in l^2(\mathbf{Z})$  is equal to the  $z$ -transform evaluated on the unit circle

$$F(\omega) = \sum_{n=-\infty}^{\infty} f(n) e^{-j\omega n},$$

and the Fourier transform of a discrete signal  $f(n_x, n_y) \in l^2(\mathbf{Z}^2)$  is defined as

$$F(\omega_x, \omega_y) = \sum_{n_x=-\infty}^{\infty} \sum_{n_y=-\infty}^{\infty} f(n_x, n_y) e^{-j(\omega_x n_x + \omega_y n_y)}.$$

For later use, we define the following functions:

1. the unit impulse function

$$\delta_u(x) := \begin{cases} 1 & \text{for } x = 0 \\ 0 & \text{otherwise,} \end{cases}$$

2. the unit step function

$$u(x) := \begin{cases} 1 & \text{for } x \geq 0 \\ 0 & \text{for } x < 0, \end{cases}$$

3. the rectangular function

$$\text{rect}(x) := \begin{cases} 1 & \text{for } |x| \leq \frac{1}{2} \\ 0 & \text{for } |x| > \frac{1}{2}, \end{cases}$$

4. the sinc function

$$\text{sinc}(x) := \frac{\sin(\pi x)}{\pi x}, \quad \text{and}$$

5. the unit impulse sequence

$$\delta(n) := \begin{cases} 1 & \text{for } n = 0 \\ 0 & \text{otherwise,} \end{cases}$$

where  $x \in \mathbf{R}$  and  $n \in \mathbf{Z}$ .

## 2 Body

### 2.1 Signal Processing Using Central B-Splines

In this section, we briefly review fundamentals of spline processing needed for derivations in Section 2.2. First, Section 2.1.1 presents basic properties of central B-splines. Next, Section 2.1.2 introduces a digital filtering scheme for B-spline signal processing. Finally, Section 2.1.3 describes signal approximations using projections onto the spline function spaces.

#### 2.1.1 Central B-Splines: Definition and Properties

Given real numbers  $-\infty \leq x_0 < x_1 < x_2 < \dots < x_m < x_{m+1} \leq \infty$ , a function on the interval  $[x_0, x_{m+1}]$  is called a spline function of order  $p$  with the knot (i.e., grid point) sequence  $x_1, x_2, \dots, x_m$ , if it is (1) a polynomial of degree  $p$  or less in each interval  $[x_i, x_{i+1}]$ ,  $i = 0, 1, \dots, m$ , and (2) continuous in its derivatives up to the order  $p-1$  on the interval  $[x_0, x_{m+1}]$  (i.e.,  $\mathbf{C}^{p-1}[x_0, x_{m+1}]$ ).

Here, we will concentrate primarily on basis splines (B-splines), or more precisely, central B-splines having knots at  $i \in \mathbf{Z}$  for  $p$  odd and at  $i + \frac{1}{2}$  for  $p$  even [13]. Central B-splines of order  $p$  (with  $p+1$  knots) are defined as

$$\beta_p(x) := \frac{1}{p!} \sum_{i=0}^{p+1} (-1)^i \binom{p+1}{i} \left(x + \frac{p+1}{2} - i\right)^p u\left(x + \frac{p+1}{2} - i\right).$$

Figure 1 shows  $\beta_p(x)$  and their Fourier transforms  $\hat{\beta}_p(\omega)$  for  $p \in \{0, 1, 2, 3, 4\}$ .

A family of functions  $\{\beta_p(x - m)\}_{m \in \mathbf{Z}}$  forms a basis of  $\mathbf{S}^p$ , a space of order  $p$  spline functions with knots at  $i$  for  $p$  odd and at  $i + \frac{1}{2}$  for  $p$  even ( $i \in \mathbf{Z}$ ) [13, 14]. Except for  $p = 0$ , the basis functions  $\{\beta_p(x - m)\}$  are not orthogonal.

Let us list some properties of functions  $\beta_p(x)$  [15, 13]:

1.  $\beta_p(x)$  are nonnegative functions with a support of length  $p+1$ ,

2.  $\beta_p(x) = \overbrace{\beta_0 * \beta_0 * \dots * \beta_0(x)}^{p+1 \text{ times}}$ , where “ $*$ ” denotes the convolution operator, or, equivalently, in the Fourier domain:

$$\hat{\beta}_p(\omega) = \left( \frac{\sin(\frac{\omega}{2})}{\frac{\omega}{2}} \right)^{p+1},$$

3.  $\beta_p(x) = \frac{1}{p} \left( \left( \frac{p+1}{2} + x \right) \beta_{p-1}\left(x + \frac{1}{2}\right) + \left( \frac{p+1}{2} - x \right) \beta_{p-1}\left(x - \frac{1}{2}\right) \right),$
4.  $\frac{\partial \beta_p(x)}{\partial x} = \beta_{p-1}\left(x + \frac{1}{2}\right) - \beta_{p-1}\left(x - \frac{1}{2}\right).$

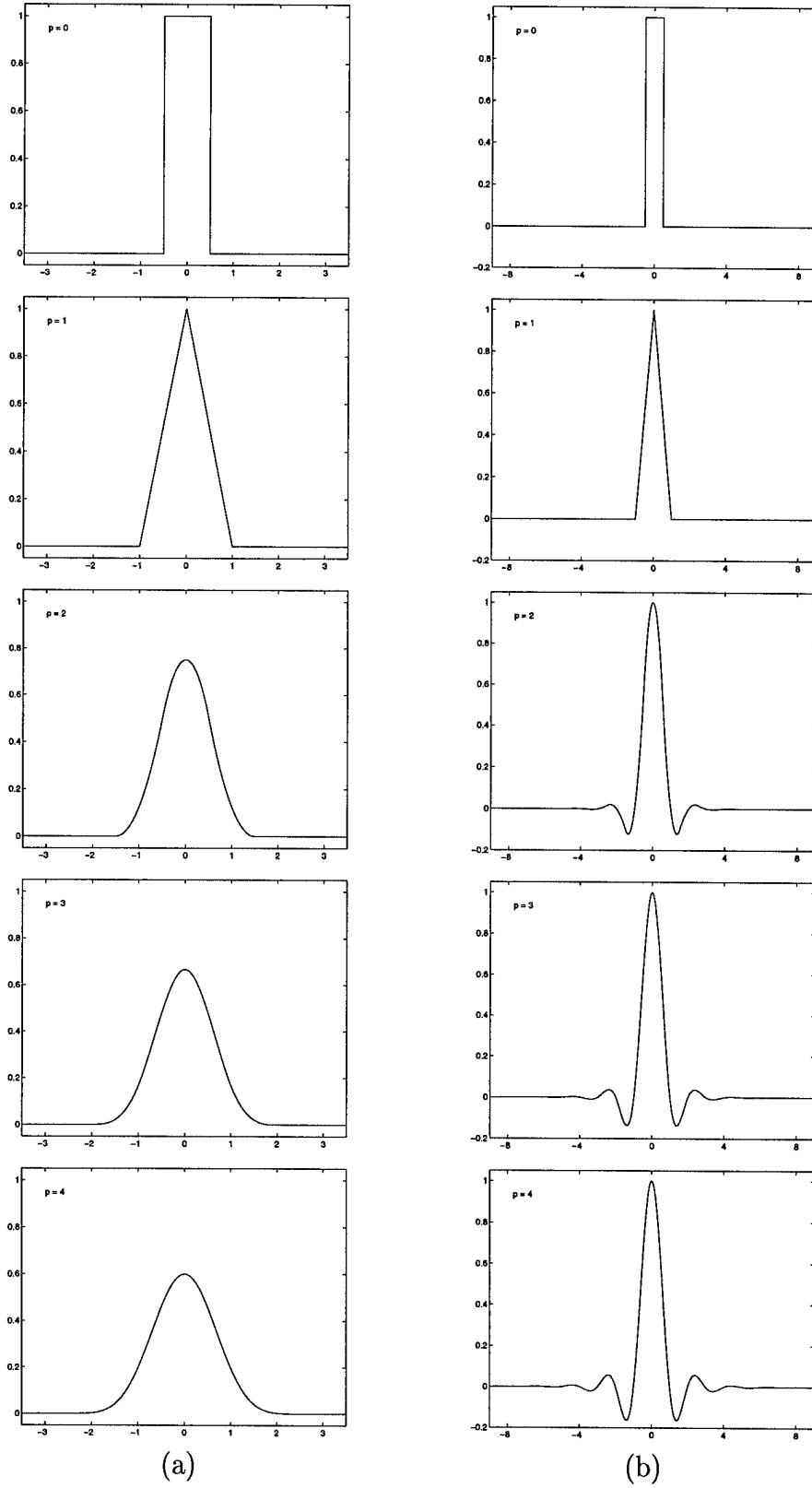


Figure 1: Spline functions (a)  $\beta_p(x)$  and (b)  $\eta_p(x)$  for  $p \in \{0, 1, 2, 3, 4\}$ .

Another interesting property of B-splines is the fact that they converge to a Gaussian as their order tends to infinity. Unser *et al.* [16] derived the Gaussian approximation

$$\beta_p(x) \simeq \frac{1}{\sqrt{2\pi}\sigma_p} e^{-\frac{x^2}{2\sigma_p^2}},$$

where  $\sigma_p = \sqrt{\frac{p+1}{12}}$ . Ratio  $\frac{\|\beta_p - \tilde{\beta}_p\|^2}{\|\beta_p\|^2}$ , for example, is already well below 0.2%.

Denoting by  $\mathbf{S}_1^p$  a spline function space spanned by  $\{\beta_p(x - m)\}$  for  $p$  odd and by  $\{\beta_p(x - \frac{1}{2} - m)\}$  for  $p$  even (subscript in  $\mathbf{S}_1^p$  refers to the fact that spline functions have knots at integers), spline spaces form a nested sequence  $\dots \subset \mathbf{S}_{2^i}^p \subset \dots \subset \mathbf{S}_2^p \subset \mathbf{S}_1^p \subset \mathbf{S}_{2^{-1}}^p \subset \dots \subset \mathbf{S}_{2^{-i}}^p \subset \dots$ . By orthogonalizing this basis functions a multiresolution analysis of  $L^2(\mathbf{R})$ , from which the Battle-Lemarié wavelet bases stem, can be built [17]. Here, we will not pursue constructions of orthogonal, semi-orthogonal, or biorthogonal spline-wavelets any further—reader looking for a detailed treatment of this subject may find a good starting point in books [18, 19].

### 2.1.2 B-Spline Signal Interpolations

Unser *et al.* developed a fast digital filtering scheme for B-spline signal processing [20]. They defined a discrete B-spline of order  $p$  and expansion factor (spacing between knots)  $m$  as

$$b_{p,m}(n) := \beta_p\left(\frac{n}{m}\right), \quad n, m \in \mathbf{Z}.$$

Henceforth, if the distance between knots equals one, we will write  $b_p(n)$  instead of  $b_{p,1}(n)$ . Interpolation of a discrete signal  $s(n) \in l^2(\mathbf{Z})$  by  $s_p(x) \in \mathbf{S}^p$  using central B-splines

$$s(n) = s_p(x) \Big|_{x=n} = \sum_{i=-\infty}^{\infty} c(i) \beta_p(x - i) \Big|_{x=n}, \quad (1)$$

can now be written as a convolution sum

$$s(n) = c * b_p(n). \quad (2)$$

If  $s(n)$  are samples of a function  $s(x)$  bandlimited to  $[-\pi, \pi]$  (i.e., the support of its Fourier transform  $S(\omega)$  is in  $[-\pi, \pi]$ ), it can be shown that  $s_p(x) \rightarrow s(x)$  as  $p \rightarrow \infty$  [21, 22].

In [20], they refer to a linear operator by which B-spline coefficients  $c(n)$  can be obtained from samples  $s(n)$  as a “direct B-spline transform.” Equation (2) therefore represents “indirect B-spline transform” of a sequence  $\{c(n)\}$ .

After taking the  $z$ -transform of (2), the direct B-spline filters are found to be

$b_p^{-1}(n) = \mathcal{Z}^{-1}\{[B_p(z)]^{-1}\}$ . Since B-spline functions  $\beta_p(x)$  are compactly supported, indirect

Table 1: Transfer functions of direct B-spline filters for orders from 0 to 9.

$p$	$B_p^{-1}(z)$
0	1
1	1
2	$\frac{8}{z+6+z^{-1}}$
3	$\frac{6}{z+4+z^{-1}}$
4	$\frac{384}{z^2+76z+230+76z^{-1}+z^{-2}}$
5	$\frac{120}{z^2+26z+66+26z^{-1}+z^{-2}}$
6	$\frac{46080}{z^3+722z^2+10543z+23548+10543z^{-1}+722z^{-2}+z^{-3}}$
7	$\frac{5040}{z^3+120z^2+1191z+2416+1191z^{-1}+120z^{-2}+z^{-3}}$
8	$\frac{10321920}{z^4+6552z^3+331612z^2+2485288z+4675014+2485288z^{-1}+331612z^{-2}+6552z^{-3}+z^{-4}}$
9	$\frac{362880}{z^4+502z^3+14608z^2+88234z+156190+88234z^{-1}+14608z^{-2}+502z^{-3}+z^{-4}}$

B-spline filters  $b_p(n)$  are finite impulse response (FIR) filters, while direct B-spline filters  $b_p^{-1}(n)$  are infinite impulse response (IIR) filters. Aldroubi *et al.* [21] showed that IIR filters  $b_p^{-1}(n)$  are stable (i.e., the region of convergence of  $B_p^{-1}(z)$  includes the unit circle [23]) for any order  $p$ . Note that both indirect and direct B-spline filters are symmetric, which follows from the fact that central B-splines  $\beta_p(x)$  are symmetric.

Table 1 shows the  $z$ -transforms of direct B-spline filters for the first ten orders. We postpone the discussion on implementation details of B-spline filters until Sections 2.2.8 and 2.2.9.

Instead of using B-spline interpolation as given by (1) it is sometimes convenient to express the interpolating function  $s_p(x)$  in terms of discrete samples  $s(n)$

$$s_p(x) = \sum_{i=-\infty}^{\infty} s(i)\eta_p(x-i), \quad (3)$$

where  $\eta_p(x)$  is the cardinal spline of order  $p$ . In the frequency domain, cardinal splines converge to an ideal lowpass filter with cutoff frequency  $\pi$  (i.e.,  $\eta_p(x) \rightarrow \text{sinc}(x)$ ) as  $p$  tends to infinity [21, 24], which establishes the asymptotic equivalence with Shannon's sampling theorem [25].

Using (1) and (2) with (3) cardinal splines can be related to B-splines:

$$\eta_p(x) = \sum_{i=-\infty}^{\infty} b_p^{-1}(i) \beta_p(x-i). \quad (4)$$

Cardinal splines  $\eta_p(x)$  and  $\hat{\eta}_p(\omega)$  for  $p \in \{0, 1, 2, 3, 4\}$  are shown in Figure 2.

### 2.1.3 B-Spline Signal Approximations

Central B-splines are also simple to use when the goal is function approximation. Least-squares B-spline approximation of  $s(x) \in L^2(\mathbf{R})$  is achieved by computing the orthogonal projection of this function onto  $\mathbf{S}^p$ . We have

$$\tilde{s}(x) = s_p(x) = \sum_{i=-\infty}^{\infty} d(i) \beta_p(x-i) \quad (5)$$

with

$$d(i) = \langle s(x), \overset{\circ}{\beta}_p(x-i) \rangle, \quad (6)$$

where

$$\overset{\circ}{\beta}_p(x) = \sum_{i=-\infty}^{\infty} b_{2p+1}^{-1}(i) \beta_p(x-i)$$

is the dual spline of order  $p$  [24]. Spline functions  $\beta_p(x)$  and  $\overset{\circ}{\beta}_p(x)$  satisfy the biorthogonality condition

$$\langle \beta_p(x-m), \overset{\circ}{\beta}_p(x-n) \rangle = \delta(m-n), \quad m, n \in \mathbf{Z}.$$

(Note that, since both  $\beta_p(x)$  and  $\overset{\circ}{\beta}_p(x)$  form a basis of  $\mathbf{S}^p$ , they can be interchanged in (5) and (6).)

Figure 3 shows functions  $\overset{\circ}{\beta}_p(x)$  and their Fourier transforms  $\hat{\overset{\circ}{\beta}}_p(\omega)$  for  $p \in \{0, 1, 2, 3, 4\}$ .

An interesting alternative to the minimum  $L^2$ -norm (i.e., least-squares) approximation of a signal is obtained by computing oblique instead of orthogonal projection of the signal onto the spline function space. Unser and Aldroubi proposed an independent specification of the sampling and approximation spaces [26]: a linear operator maps coefficients of the input signal expansion over sampling space basis into the coefficients of the approximation space basis expansion from which the signal's projection onto the approximation space is recovered. Constraining the entire system to be linear, shift-invariant for integer translations, and consistent (i.e., the system acts as an identity operator for functions that belong to the approximation space), the obtained solution for the signal approximation is



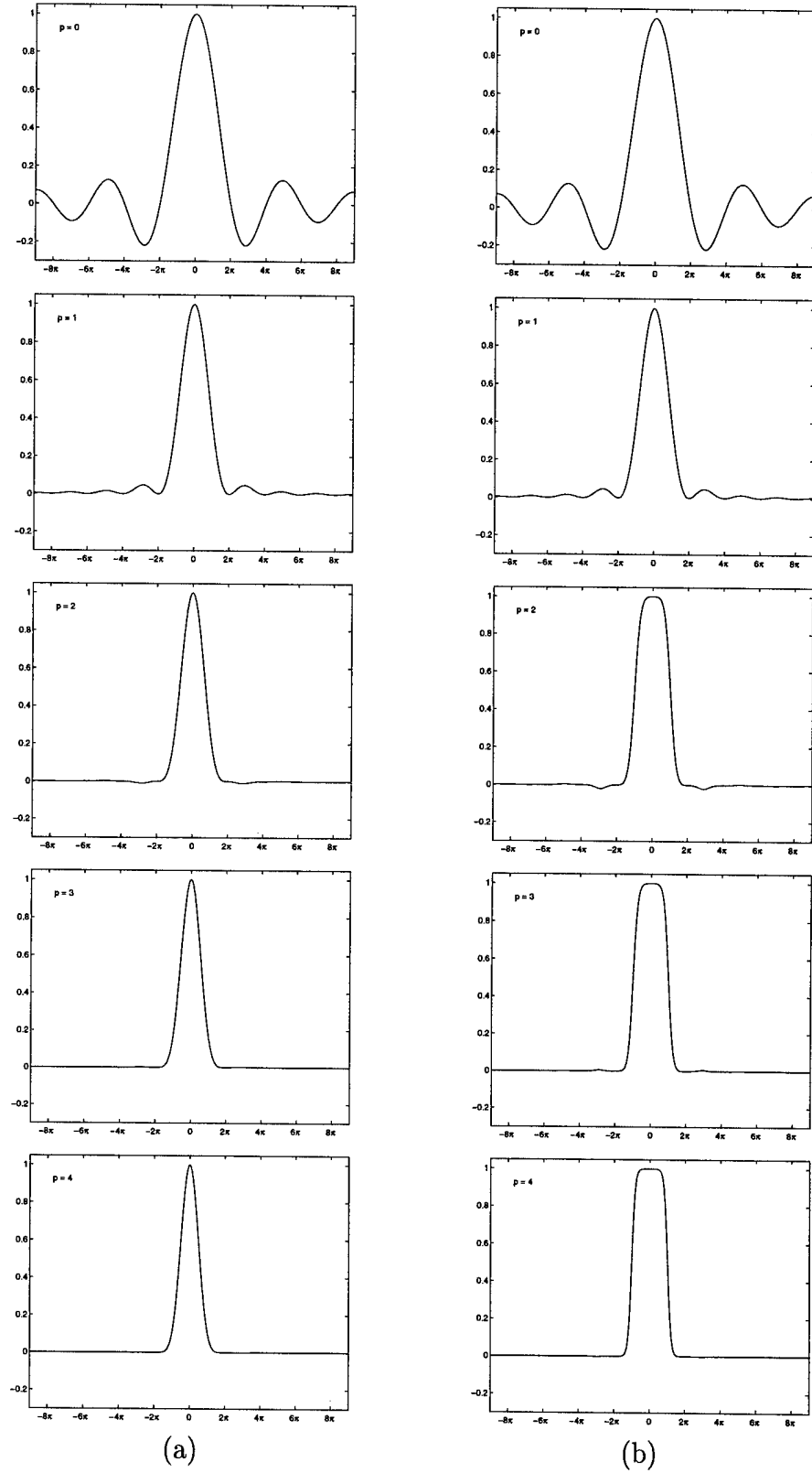


Figure 2: Fourier transforms of spline functions (a)  $\hat{\beta}_p(\omega)$  and (b)  $\hat{\eta}_p(\omega)$  for  $p \in \{0, 1, 2, 3, 4\}$ .

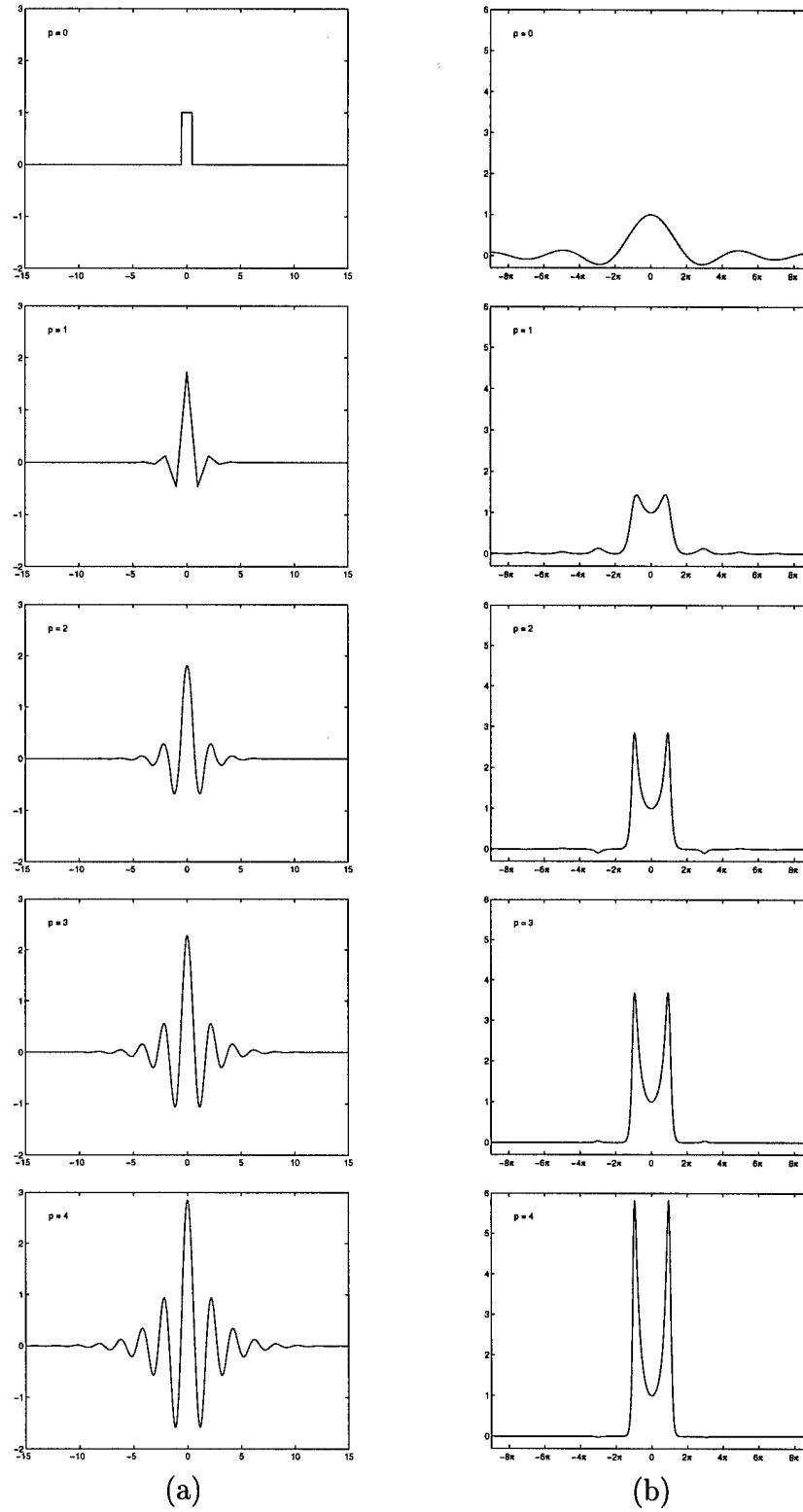


Figure 3: Spline functions (a)  $\hat{\beta}_p(x)$  and (b) their respective Fourier transforms  $\hat{\beta}_p(\omega)$  for  $p \in \{0, 1, 2, 3, 4\}$ .

the projection of a signal onto the approximation space perpendicular to the sampling space [26]. Analogously to (5) and (6) this projection can be expressed as

$$s_r(x) = \sum_{i=-\infty}^{\infty} a(i)\beta_r(x-i) \quad (7)$$

with

$$a(i) = q_{12}^{-1} * \langle s(x), \beta_s(x-i) \rangle,$$

where  $q_{12}^{-1}$  is the convolution inverse of the cross-correlation sequence

$$q_{12}(i) = \langle \beta_s(x-i), \beta_r(x) \rangle = b_{s+r+1}(i).$$

When the sampling space  $\mathbf{S}^s$  and the approximation space  $\mathbf{S}^r$  are identical (i.e.,  $s=r$ ), an orthogonal projection given by (5) and (6) results. (Note that the described oblique projection is not restricted to spline function spaces—the only requirement is that both sampling space basis and approximation space basis are Riesz bases of the corresponding function spaces [26].)

Signal approximation (7) is particularly attractive in situations where the sampling space is given *a priori* (e.g., by the impulse response of the acquisition device [26]) or when such an approximation is close to the optimal least-squares solution but simpler to implement than the orthogonal projection (e.g., [27]).

## 2.2 Steerable Dyadic Transforms

In this section, we derive transforms that will enable efficient directional processing of mammograms. Section 2.2.1 deals with problems due to the lack of translation and rotation invariance of orthogonal and biorthogonal wavelet transforms. In Section 2.2.2, the one-dimensional discrete dyadic wavelet transform [11] is augmented to obtain a strong foundation for derivations of two-dimensional transforms. Connections to reconstruction from edges, and to scale-space filtering are mentioned in Section 2.2.3. Section 2.2.4 presents a direct extension of the one-dimensional transform to two dimensions.<sup>1</sup> The concept of steerability is explained in Section 2.2.5, and then used for derivations of a steerable dyadic wavelet transform and multiscale spline derivative-based transform in Sections 2.2.6 and 2.2.7, respectively. Sections 2.2.8 and 2.2.9 describe how to exploit symmetries of signals and filters for a fast implementation of the transforms.

---

<sup>1</sup>For extensions to higher dimensions, please refer to [12, 28].

### 2.2.1 Shortcomings of Traditional Methods of Wavelet Analysis

Analyzing images across multiple scales and resolution has become a powerful tool for solving compelling problems in computational vision, image processing, and pattern recognition. Wavelet theory encompasses multiscale and multiresolution representations, such as subband filtering [29], image pyramids [30], and scale space filtering [31], into a unified mathematical framework. In the area of image processing, there remain few research areas to which wavelet analysis has not been applied. For example, problems in image compression, denoising, restoration, enhancement, registration, fusion, segmentation, and analysis, have all been approached with distinct kinds of wavelet processing.

Though ubiquitous, wavelet analysis is not without problems of its own. Lack of translation invariance, one of the major problems of the wavelet transform [17], is in multiple dimensions accompanied with lack of rotation invariance.

Wavelet transform in its most commonly used orthogonal or biorthogonal forms is not translation and rotation-invariant. By translation-invariant transform, we mean a transform that commutes with a translation operator. Since we will deal primarily with discrete transforms in this work, we constrain the translation parameter to integer multiples of a sampling period.

Lack of translation invariance of the discrete wavelet transform is illustrated in Figure 4. Here, we can clearly see how a translation of the input signal by one sample results in a completely different set of transform coefficients (orthogonal wavelet DAUB4<sup>2</sup> [17] was used in this experiment).

Noninvariance under translations of an orthogonal and biorthogonal wavelet transform is due to lower sampling density at coarser scales.<sup>3</sup> A straightforward way of dealing with this problem is to construct a redundant transform by using the same sampling frequency for the input signal and all scales of the transform. A filter bank implementation of such a transform, called “*algorithme à trous*” [32], is based upon the fact that downsampling followed by filtering is equivalent to filtering with the upsampled filter before the downsampling, as shown in Figure 5.

Lack of rotation invariance is another shortcoming of traditional (i.e., orthogonal and biorthogonal) wavelet techniques. In defining rotation invariance, we are a bit less strict than with translation invariance. We do not require that the transform commutes with a rotation operator here. Even in the case of a simple filtering, this would limit us to

---

<sup>2</sup>The number in DAUB4 refers to twice the order of the wavelet (i.e., two in this case).

<sup>3</sup>In practice, since analysis is performed over a finite range of scales, a discrete wavelet transform is translation-invariant by translations determined by the coarsest scale (e.g., sixteen samples for the analysis from Figure 4) [17].

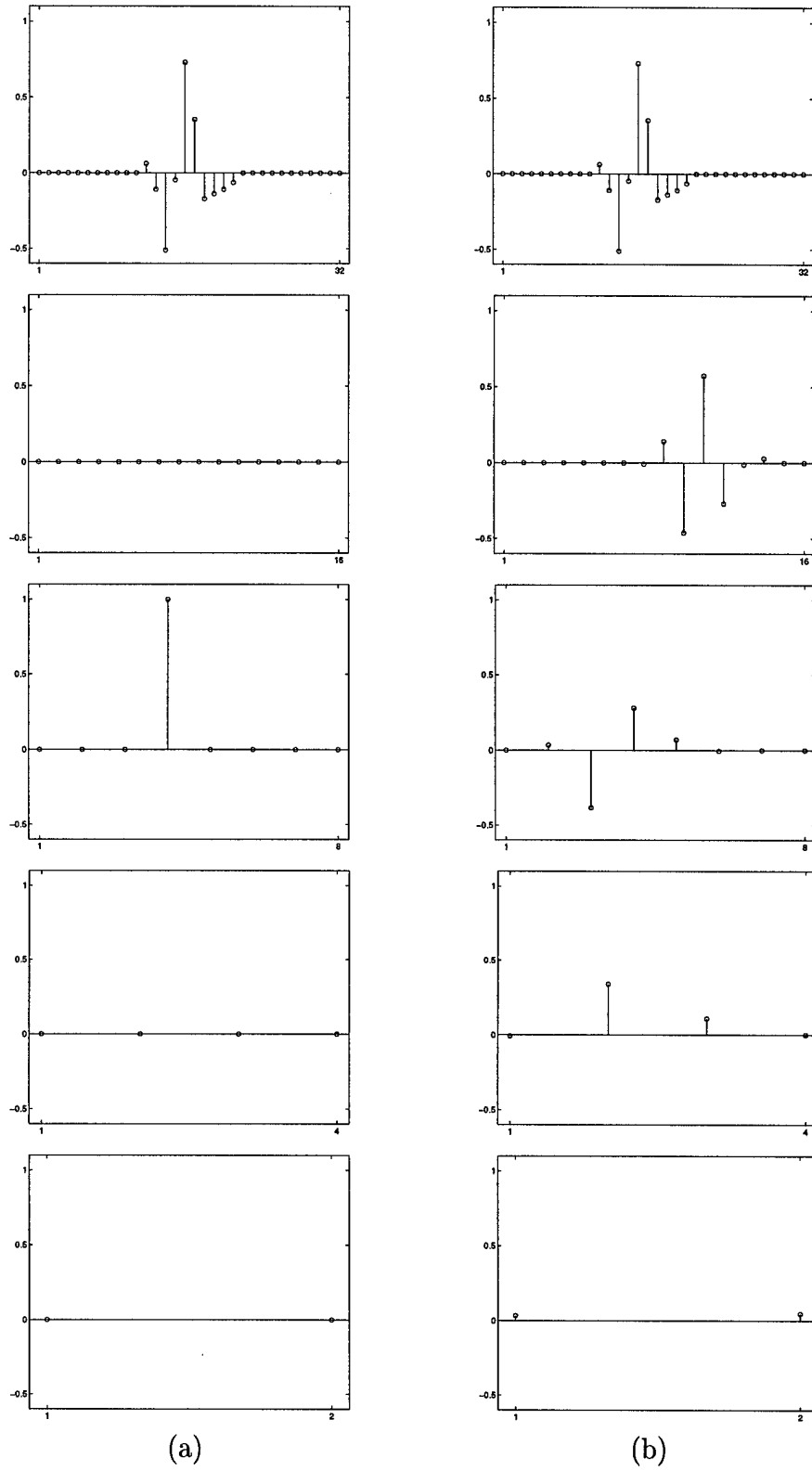


Figure 4: (a) Original signal and (b) signal translated one sample to the left with its discrete wavelet transform coefficients shown across dyadic scales  $2^m$ ,  $m \in \{1, 2, 3, 4\}$ .

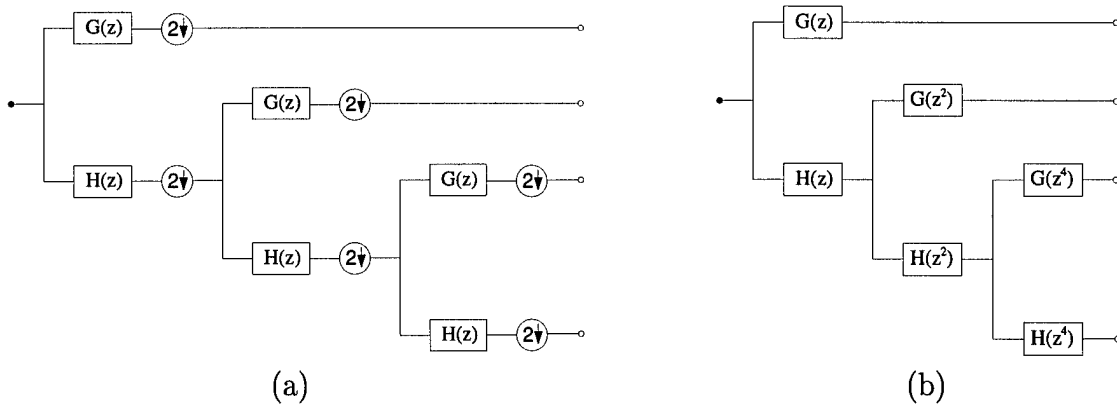


Figure 5: Filter bank implementation for (a) a discrete wavelet transform and (b) “algorithm à trous” decompositions for three levels of analysis.

circularly symmetric filters only. Our requirement for analysis is a transform that enables rotation-invariant processing. As an example of such a transform, let us consider filtering with the first derivative of a two-dimensional Gaussian probability density function in two directions, specifically, along  $x$  and along  $y$ -axis. By linearly combining the results of filtering in these two directions, filtering with the first derivative of a Gaussian in any direction can be computed. This fact was used by Canny [33] for edge detection. A determined edge direction rotates as an input image is rotated.

After choosing the fundamental properties of the transform, one must decide upon the basis functions to be applied. For our studies, we selected basis functions that well approximated derivatives of a Gaussian, because (1) the Gaussian probability density function is optimally concentrated in both time and frequency domain, and thus suitable for time-frequency analysis, (2) higher order derivatives of a Gaussian can be, similar to the first derivative, used for rotation-invariant processing [34], and (3) the Gaussian function generates a causal (in a sense that a coarse scale depends exclusively on the previous finer scale) scale space [35]. The last property makes possible scale-space “tracking” of emergent features.

### 2.2.2 1-D Discrete Dyadic Wavelet Transform Revisited

A discrete wavelet transform is obtained from a continuous representation by discretizing dilation and translation parameters such that the resulting set of wavelets constitutes a frame. The dilation parameter is typically discretized by an exponential sampling with a fixed dilation step and the translation parameter by integer multiples of a fixed step [17]. Unfortunately, the resulting transform is variant under translations, a property which makes it less attractive for image analysis.

As we have already mentioned in Section 2.2.1, sampling the translation parameter with the same sampling period as the input function to the transform results in a translation-invariant, but redundant representation. The dyadic wavelet transform proposed by Mallat and Zhong [11] is one such representation. Let us begin with a brief review of properties of the dyadic wavelet transform as described in [11], but included here for completeness.

The dyadic wavelet transform of a function  $s(x) \in L^2(\mathbf{R})$  is defined as a sequence of functions

$$\{W_m s(x)\}_{m \in \mathbf{Z}}, \quad (8)$$

where  $W_m s(x) = s * \psi_m(x)$ , and  $\psi_m(x) = 2^{-m} \psi(2^{-m}x)$  is a wavelet  $\psi(x)$  expanded by a dilation parameter (or scale)  $2^m$ . Note the use of convolution instead of an inner product. To ensure coverage of the frequency axis the requirement on the Fourier transform of  $\psi_m(x)$  is the existence of  $A_1 > 0$  and  $B_1 < \infty$  such that

$$A_1 \leq \sum_{m=-\infty}^{\infty} |\hat{\psi}(2^m \omega)|^2 \leq B_1$$

is satisfied almost everywhere. The constraint on the Fourier transform of the (nonunique) reconstructing function  $\chi(x)$  is

$$\sum_{m=-\infty}^{\infty} \hat{\psi}(2^m \omega) \hat{\chi}(2^m \omega) = 1.$$

A function  $s(x)$  can then be completely reconstructed from its dyadic wavelet transform using the identity

$$s(x) = \sum_{m=-\infty}^{\infty} W_m s * \chi_m(x),$$

where  $\chi_m(x) = 2^{-m} \chi(2^{-m}x)$ .

In numerical applications, processing is performed on discrete rather than continuous functions. When the function to be transformed is in the discrete form, the scale  $2^m$  can no longer vary over all  $m \in \mathbf{Z}$ . Finite sampling rate prohibits the scale from being arbitrarily small, while computational resources restrict the use of an arbitrarily large scale. Let the finest scale be normalized to 1 and the coarsest scale set to  $2^M$ .

The smoothing of a function  $s(x) \in L^2(\mathbf{R})$  is defined as

$$S_m s(x) = s * \phi_m(x),$$

where  $\phi_m(x) = 2^{-m} \phi(2^{-m}x)$  with  $m \in \mathbf{Z}$ , and  $\phi(x)$  is a smoothing function (i.e., its integral is equal to 1 and  $\phi(x) \rightarrow 0$  as  $|x| \rightarrow \infty$ ).

In [11], a real smoothing function  $\phi(x)$  was selected, whose Fourier transform satisfied

$$|\hat{\phi}(\omega)|^2 = \sum_{m=1}^{\infty} \hat{\psi}(2^m \omega) \hat{\chi}(2^m \omega). \quad (9)$$

In addition, it was shown that any discrete function of finite energy  $s(n) \in l^2(\mathbf{Z})$  can be written as the uniform sampling of some function smoothed at scale 1, i.e.,  $s(n) = S_0 f(n)$ , where  $f(x) \in L^2(\mathbf{R})$  is not unique. Thus, the discrete dyadic wavelet transform of  $s(n)$  for any coarse scale  $2^M$  was defined as a sequence of discrete functions

$$\{S_M f(n+s), \{W_m f(n+s)\}_{m \in [1, M]}\}_{n \in \mathbf{Z}},$$

where  $s$  is a  $\psi(x)$  dependent sampling shift.

The above initialization  $s(n) = S_0 f(n)$  is rather standard in the discrete wavelet transform computation [17], although it yields correct results (i.e., the discrete wavelet transform is equal to the samples of its continuous counterpart) only when  $s(n) = S_0 s(n)$ . Here, we will concentrate on wavelets which are derivatives of spline functions and this will lead us to a simple initialization procedure [36] that alleviates the above problem.

For a certain choice of wavelets the discrete dyadic wavelet transform can be implemented within a fast hierarchical digital filtering scheme. Next, we shall summarize the relations between filters, wavelets, and smoothing functions.

First, let us introduce a real smoothing function  $\varphi(x)$  such that (9) can be rewritten as<sup>4</sup>

$$\hat{\phi}(\omega) \hat{\varphi}(\omega) = \sum_{m=0}^{\infty} \hat{\psi}(2^m \omega) \hat{\chi}(2^m \omega), \quad (10)$$

and let us set  $\phi(x) = \beta_p(x)$  (i.e., we restrict ourselves to wavelets which are spline functions).

Computing (10) for the finest two scales shows that

$$\hat{\psi}(\omega) \hat{\chi}(\omega) = \hat{\beta}_p(\omega) \hat{\varphi}(\omega) - \hat{\beta}_p(2\omega) \hat{\varphi}(2\omega). \quad (11)$$

$\hat{\beta}_p(2\omega)$  can be related to  $\hat{\beta}_p(\omega)$  by expressing  $\hat{\beta}_p(2\omega)$  as (cf. Proposition 1 of [36])

$$\hat{\beta}_p(2\omega) = \frac{1}{2^{p+1}} \left( \frac{\sin(\omega)}{\sin(\frac{\omega}{2})} \right)^{p+1} \left( \frac{\sin(\frac{\omega}{2})}{\frac{\omega}{2}} \right)^{p+1},$$

and using  $\sum_{m=0}^M e^{j(m\omega+\theta)} = \frac{\sin(\frac{(M+1)\omega}{2})}{\sin(\frac{\omega}{2})} e^{j(\frac{M\omega}{2}+\theta)}$ :

$$\hat{\beta}_p(2\omega) = \left( \cos\left(\frac{\omega}{2}\right) \right)^{p+1} \hat{\beta}_p(\omega). \quad (12)$$

---

<sup>4</sup>Note that the sum index determines the range of scales of the discrete transform: using (9) we have  $\hat{\psi}(2\omega)$  and  $\hat{\chi}(2\omega)$  at the finest scale of the transform, while for (10) we get  $\hat{\psi}(\omega)$  and  $\hat{\chi}(\omega)$ .



(Note that a relation similar to (12) can be derived for integer scales provided that the dilation parameter and the order  $p$  are not both even [36].)

Let  $F(\omega)$  be a digital filter frequency response and let  $F_s(\omega) = e^{j\omega s} F(\omega)$ .

If we choose

$$\hat{\psi}(\omega) = G_{-s}(\omega) \hat{\beta}_p(\omega), \quad (13)$$

$$\hat{\varphi}(2\omega) = L_s(\omega) \hat{\varphi}(\omega), \quad (14)$$

$$\hat{\chi}(\omega) = K_s(\omega) \hat{\varphi}(\omega), \quad (15)$$

and

$$H(\omega) = e^{j\omega s} \left( \cos \left( \frac{\omega}{2} \right) \right)^{p+1}, \quad (16)$$

where  $s \in \{0, \frac{1}{2}\}$  is a filter dependent sampling shift needed for  $g(n)$ ,  $l(n)$ ,  $k(n)$ , and  $h(n)$  to be FIR filters, and insert Equations (12)–(16) into (11), we observe the relation between frequency responses of the filters

$$G(\omega)K(\omega) + H(\omega)L(\omega) = 1. \quad (17)$$

Similar to orthogonal and biorthogonal discrete wavelet transforms, the discrete dyadic wavelet transform can be implemented within a hierarchical filtering scheme. To derive such a digital filtering scheme, let us assume that  $\hat{s}(\omega)$  from (8) is bandlimited to  $[-\pi, \pi]$ . Using Shannon's sampling theorem [25] and (13) in the definition of the dyadic wavelet transform (8) with  $m=0$  shows

$$W_0 s(x) = \int_{-\infty}^{\infty} \sum_{i=-\infty}^{\infty} s(i) \text{sinc}(t-i) \sum_{m=-\infty}^{\infty} g_{-s}(m) \beta_p(x-t-m) dt.$$

By making use of the fact that the cardinal spline functions tend to the sinc function as their order  $r$  approaches infinity, and employing (4) we can write

$$\widehat{W_0 s}(\omega) \simeq S(\omega) B_r^{-1}(\omega) \hat{\beta}_r(\omega) \hat{\beta}_p(\omega) G_{-s}(\omega),$$

or, by using (12) and (16),

$$\mathcal{F}\{W_m s(x)|_{x=n}\} \simeq S(\omega) B_r^{-1}(\omega) B_{p+r+1}(\omega) G_{-s}(2^m \omega) \prod_{i=0}^{m-1} H_{-s}(2^i \omega). \quad (18)$$

Equation (18) entirely specifies the discrete dyadic wavelet transform decomposition, while the reconstruction follows from (11)–(16). Three levels of a filter bank implementation are shown in Figure 6. (Note that the initialization is the same as the one proposed in [36] and that except for the prefiltering and postfiltering, this scheme is implementing “algorithme à

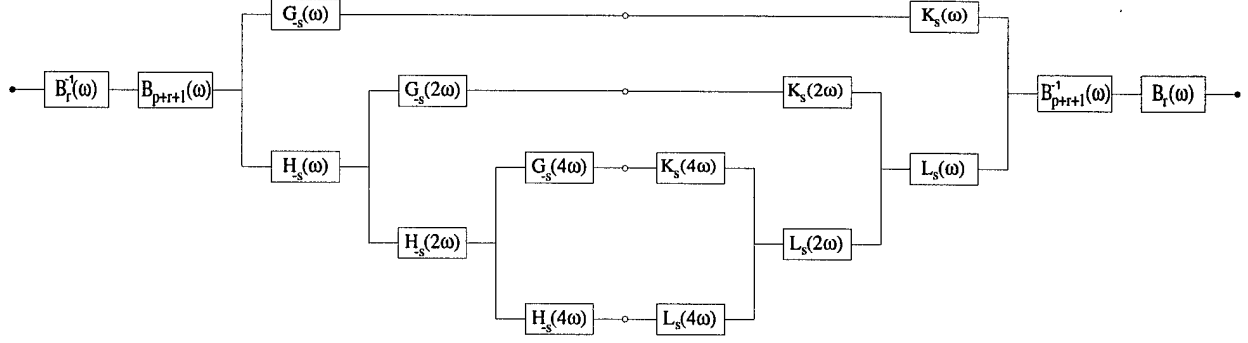


Figure 6: Filter bank implementation of a one-dimensional discrete dyadic wavelet transform decomposition (left) and reconstruction (right) for three levels of analysis.

trous.”) Noninteger shifts at scale 1 for filters with  $s = \frac{1}{2}$  are rounded to the nearest integer.

We will now perform a simple experiment which will illustrate the difference between the implementation of the discrete dyadic wavelet transform as originally proposed in [11] (i.e., without prefiltering and postfiltering) and the one from Figure 6.

Let  $s(x) = \text{sinc}(x)$ ,  $p = 2$ , and  $g(n) = 2\delta(n+1) - 2\delta(n)$  (this particular choice for  $p$  and  $g(n)$  results in the same wavelet as was used by Mallat and collaborators [37, 11]). The dyadic wavelet transform of  $s(x)$  at a scale  $2^m$  (8) in the frequency domain is then

$$\widehat{W_m s}(\omega) = G_{-s}(2^m \omega) \hat{\beta}_2(2^m \omega) \text{rect}\left(\frac{\omega}{2\pi}\right). \quad (19)$$

The Fourier transform of the discrete dyadic wavelet transform of  $s(n) = \delta(n)$  at a scale  $2^m$  using spline based initialization follows from (18)

$$\mathcal{F}\{\widetilde{W_m s}(n)\} = B_r^{-1}(\omega) B_{r+3}(\omega) G_{-s}(2^m \omega) \prod_{i=0}^{m-1} H_{-s}(2^i \omega), \quad (20)$$

while the one using the algorithm from [11] equals

$$\mathcal{F}\{\widetilde{W_m s}(n)\} = G_{-s}(2^m \omega) \prod_{i=0}^{m-1} H_{-s}(2^i \omega). \quad (21)$$

In Figure 7 a comparison of magnitudes of (20) and (21) versus (19) is shown: in Figure 7(a) magnitudes of (19) (solid) and (21) (dashed) are plotted for  $m \in \{0, 1, 2, 3\}$ , while the dashed curves in 7(b) represent magnitudes of (20) with  $r = 5$ .

By choosing the appropriate order  $r$ , (20) can approximate (19) in the interval  $[-\pi, \pi]$  arbitrarily good, while originally proposed (21) has troubles at finer scales. Mallat and Zhong [11] noticed that there was a problem with their discrete transform computation, and introduced a set of constants associated with the discrete transform coefficients at

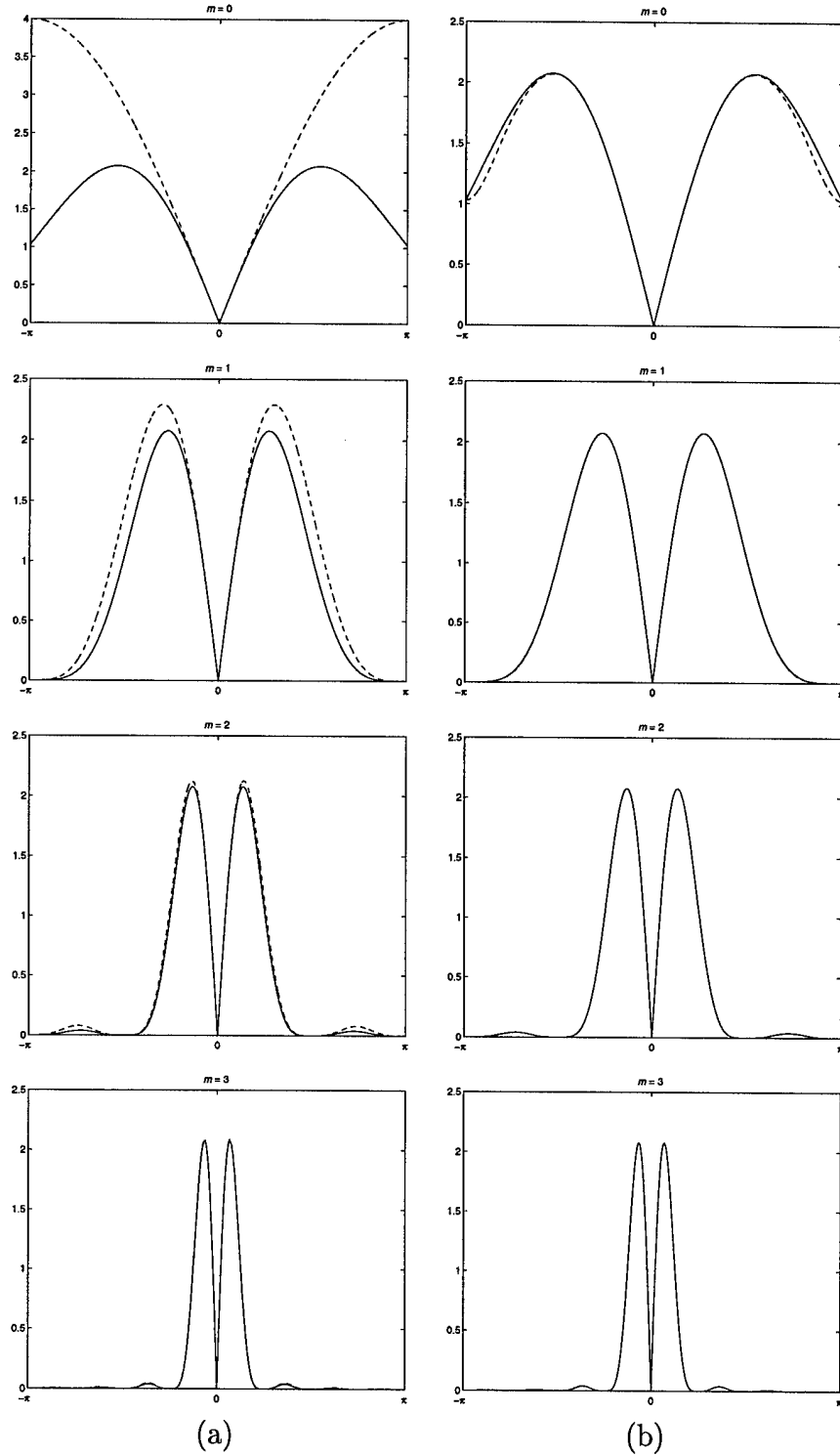


Figure 7: (a) Fourier transform magnitudes of the dyadic wavelet transform of  $s(x) = \text{sinc}(x)$  (solid) and the originally proposed discrete dyadic wavelet transform [11] of  $s(n) = \delta(n)$  (dashed). (b) Fourier transform magnitudes of the dyadic wavelet transform of  $s(x)$  (solid) and the discrete dyadic wavelet transform using quintic splines for interpolation of  $s(n)$  (dashed).

dyadic scales. They chose the values of constants such that the transform coefficient modulus maxima remained constant over all dyadic scales for a step edge input signal. In relation to Figure 7(a) this is equivalent to multiplying  $\mathcal{F}\{\widetilde{W}_m s(n)\}$  by a distinct constant for each  $m$ . Clearly, this can improve over the situation depicted by Figure 7(a), but can still not compete with the described spline based initialization.

Next, we will choose filters in the filter bank implementation of the discrete dyadic wavelet transform. As already mentioned, we are interested in wavelets which are derivatives of spline functions.  $G(\omega)$  in (13) is therefore the Fourier transform of the difference operator centered around  $-s$  (cf. Property 4 in Section 2.1):

$$G(\omega) = e^{j\omega s} \left( 2j \sin \left( \frac{\omega}{2} \right) \right)^d, \quad (22)$$

where  $d$  is the order of the derivative and the sampling shift for this filter is  $s = \frac{d \bmod 2}{2}$ .

Since  $H(\omega)$  was already given by (16), the remaining two filters to be determined are  $L(\omega)$  and  $K(\omega)$ . Both of them are (as is true for  $\varphi(x)$  and  $\chi(x)$ ) nonunique.

If we choose  $L(\omega)$  such that we can express  $K(\omega)$  in terms of a finite geometric series having the smallest number of elements for an arbitrary  $p$ , we get

$$L(\omega) = e^{-j\omega s} \sum_{m=1}^{\lfloor \frac{d+1}{2} \rfloor} (-1)^{m+1} \binom{\lfloor \frac{d+1}{2} \rfloor}{m} \left( \cos \left( \frac{\omega}{2} \right) \right)^{(p+1)(2m-1)} \quad (23)$$

and

$$K(\omega) = \frac{1}{(2j)^d} \left( e^{-j\omega s} \sin \left( \frac{\omega}{2} \right) \right)^{d \bmod 2} \left( \sum_{m=0}^p \left( \cos \left( \frac{\omega}{2} \right) \right)^{2m} \right)^{\lfloor \frac{d+1}{2} \rfloor}, \quad (24)$$

where  $\lfloor x \rfloor$  denotes the largest integer smaller than  $x$ , the sampling shift for  $L(\omega)$  is the same as the one for  $H(\omega)$  (i.e.,  $s = \frac{(p+1) \bmod 2}{2}$ ), and the sampling shift for  $K(\omega)$  is the same as the one for  $G(\omega)$ .

Note that Equations (16) and (22)–(24) work fine from the mathematical point of view, but in practice the reconstruction may become cumbersome when both  $p$  and  $d$  are large (the lengths of impulse responses  $h(n)$ ,  $g(n)$ ,  $l(n)$ , and  $k(n)$  are  $p+2$ ,  $d+1$ ,  $(p+1)(d-(d+1) \bmod 2)+1$ , and  $pd+(p+1)(d \bmod 2)+1$ , respectively, while for the frequency responses of the decomposition filters we observe that  $\lim_{p \rightarrow \infty} |H_{-s}(\omega)| = \delta_u(\omega + 2n\pi)$  and  $\lim_{d \rightarrow \infty} (2j)^{-d} |G_{-s}(\omega)| = \delta_u(\omega + (2n+1)\pi)$  with  $n \in \mathbf{Z}$ ).

It is also worth noting that  $K(\omega)$  is a lowpass filter when  $p$  is even (i.e., the reconstruction function  $\chi(x)$  is a wavelet only for  $p$  odd).

Tables 2, 3, and 4 list impulse responses of the four filters for  $p \in \{0, 1, 2\}$  and  $d \in \{1, 2, 3\}$ , while Figure 8 shows wavelets  $\psi(x) = \frac{d^d \beta_{p+d}(x)}{dx^d}$  for the same values of  $p$  and  $d$ . Wavelets

Table 2: Impulse responses  $h(n)$ ,  $g(n)$ ,  $l(n)$ , and  $k(n)$  for  $p=0$  and  $d \in \{1, 2, 3\}$ .

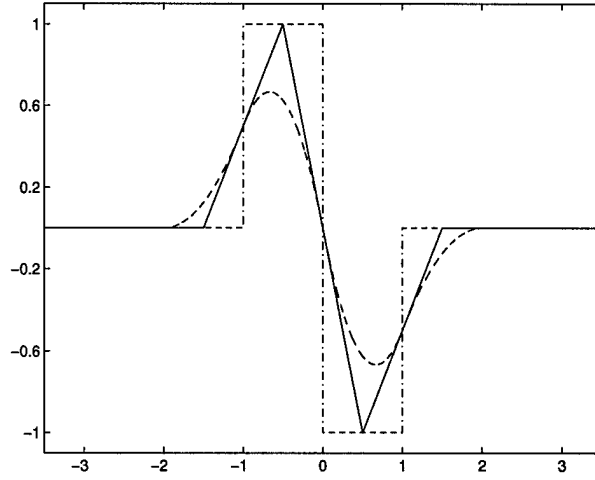
$n$	$h(n)$	$d = 1$			$d = 2$			$d = 3$		
		$g(n)$	$l(n)$	$k(n)$	$g(n)$	$l(n)$	$k(n)$	$g(n)$	$l(n)$	$k(n)$
-2								1		
-1	0.5	1			1			-3	-0.125	
0	0.5	-1	0.5	-0.25	-2	0.5	-0.25	3	0.625	0.0625
1			0.5	0.25	1	0.5		-1	0.625	-0.0625
2								-0.125		

Table 3: Impulse responses  $h(n)$ ,  $g(n)$ ,  $l(n)$ , and  $k(n)$  for  $p=1$  and  $d \in \{1, 2, 3\}$ .

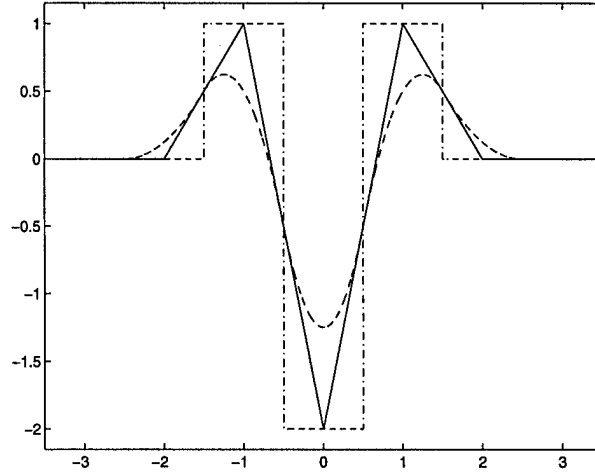
$n$	$h(n)$ $l(n)$	$d = 1$		$d = 2$	
		$g(n)$	$k(n)$	$g(n)$	$k(n)$
-1	0.25	1	-0.0625	1	-0.0625
0	0.5	-1	-0.3125	-2	-0.375
1	0.25		0.3125	1	-0.0625
2			0.0625		

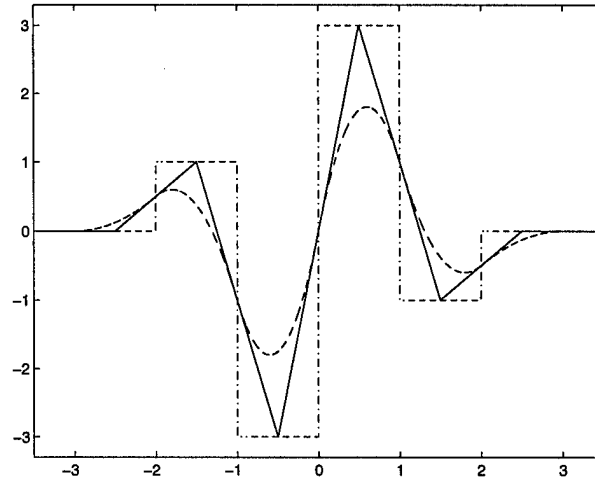
$n$	$d = 3$			
	$h(n)$	$g(n)$	$l(n)$	$k(n)$
-3			-0.015625	
-2		1	-0.09375	0.00390625
-1	0.25	-3	0.265625	0.04296875
0	0.5	3	0.6875	0.1015625
1	0.25	-1	0.265625	-0.1015625
2			-0.09375	-0.04296875
3			-0.015625	-0.00390625



(a)



(b)



(c)

Figure 8: (a) Wavelets (a)  $\psi(x) = \frac{d\beta_{p+1}(x)}{dx}$ , (b)  $\psi(x) = \frac{d^2\beta_{p+2}(x)}{dx^2}$ , and (c)  $\psi(x) = \frac{d^3\beta_{p+3}(x)}{dx^3}$  for  $p=0$  (dashdotted),  $p=1$  (solid), and  $p=2$  (dashed).

Table 4: Impulse responses  $h(n)$ ,  $g(n)$ ,  $l(n)$ , and  $k(n)$  for  $p=2$  and  $d \in \{1, 2, 3\}$ .

$n$	$h(n)$	$d = 1$			$d = 2$		
		$g(n)$	$l(n)$	$k(n)$	$g(n)$	$l(n)$	$k(n)$
-2	0.125			-0.015625			-0.015625
-1	0.375	1	0.125	-0.109375	1	0.125	-0.125
0	0.375	-1	0.375	-0.34375	-2	0.375	-0.46875
1	0.125		0.375	0.34375	1	0.375	-0.125
2			0.125	0.109375		0.125	-0.015625
3				0.015625			

$n$	$d = 3$			
	$h(n)$	$g(n)$	$l(n)$	$k(n)$
-4			-0.001953125	0.000244140625
-3			-0.017578125	0.003662109375
-2	0.125	1	-0.0703125	0.0263671875
-1	0.375	-3	0.085937	0.0908203125
0	0.375	3	0.50390625	0.13037109375
1	0.125	-1	0.50390625	-0.13037109375
2			0.0859375	-0.0908203125
3			-0.0703125	-0.0263671875
4			-0.017578125	-0.003662109375
5			-0.001953125	-0.000244140625

from this family have a support of length  $d+p+1$ , regularity order  $p$ , and are either symmetric or antisymmetric.

As already discussed, wavelets with  $p=2$  and  $d=1$  from a family of wavelets with  $p$  even and  $d=1$  were used in [37, 11], whereas filters with  $p=1$  and  $d=2$  from a family of filters with  $p$  odd and  $d=2$  were employed by Laine and collaborators [10, 8, 7]. Here described transform puts no restrictions on the choice of  $p$  or  $d$  whatsoever, and uses a better initialization procedure than the one originally proposed in [11].

### 2.2.3 Remarks

1. As mentioned in Section 2.2.1, the translation invariance property of the discrete dyadic wavelet transform is due to the fact that the translation parameter is sampled with the same sampling period as the input signal over all scales. When comparing Figure 6 to traditional filter bank implementations of an orthogonal and biorthogonal wavelet transform, we observe that each subband shown in Figure 6 is retained at its original density rather than being critically sampled. Note, that the filters at distinct scales are not the same as in orthogonal or biorthogonal cases of analysis [17].

The discrete dyadic wavelet transform is highly redundant. To obtain a more parsimonious

representation we may sample the translation parameter in a translation-invariant manner (e.g., sampling a function at its extrema or extrema of its derivatives). Of importance is, whether or not it remains possible to reconstruct the original signal from this subset of transform coefficients.

In [37, 11] a reconstruction algorithm is presented that reconstructs an approximation of a signal given the position of local maxima of wavelet coefficients modulus and the values of wavelet coefficients at each corresponding location. Wavelets with  $d=1$  were used so that the locations of maxima corresponded to inflection points of the original signal smoothed at dyadic scales.

2. For cases, when the wavelet  $\psi(x)$  from Section 2.2.2 is equal to either the first ( $d=1$ ) or the second ( $d=2$ ) derivative of a smoothing function  $\vartheta(x) = \beta_{p+d}(x)$  the dyadic wavelet transform of a function  $s(x) \in L^2(\mathbf{R})$  can be written as

$$W_m s(x) = s * \left( 2^{md} \frac{d^d \vartheta_m}{dx^d} \right) (x) = 2^{md} \frac{d^d}{dx^d} (s * \theta_m)(x) \quad m \in \mathbf{Z}, \quad d \in \{1, 2\}.$$

Depending on the wavelet selected for analysis, the wavelet transform  $W_m s(x)$  is proportional either to the first or second derivative of  $s(x)$  smoothed by  $\theta_m$ . By recording the zero-crossings of  $W_m s(x)$  for  $d=2$ , a scale-space image of the representation similar to [31] can be obtained. The only differences are that curves in the scale-space plane are computed for dyadic scales only and that  $\vartheta_m$  is a close approximation of a Gaussian instead of a true Gaussian.

#### 2.2.4 2-D Discrete Dyadic Wavelet Transform Revisited

The dyadic wavelet transform of a function  $s(x, y) \in L^2(\mathbf{R}^2)$  is defined as a set of functions [11]

$$\{W_m^1 s(x, y), W_m^2 s(x, y)\}_{m \in \mathbf{Z}}, \quad (25)$$

where  $W_m^i s(x, y) = s * \psi_m^i(x, y)$  for  $i = \{1, 2\}$  and  $\psi_m^i(x, y) = 2^{-2m} \psi^i(2^{-m}x, 2^{-m}y)$  are wavelets  $\psi^i(x, y)$  expanded by a dilation parameter  $2^m$ .

To ensure coverage of the frequency space there must exist an  $A_2 > 0$  and  $B_2 < \infty$  such that

$$A_2 \leq \sum_{m=-\infty}^{\infty} \sum_{i=1}^2 |\hat{\psi}^i(2^m \omega_x, 2^m \omega_y)|^2 \leq B_2$$

is satisfied almost everywhere. If (nonunique) functions  $\chi^1(x, y)$ ,  $\chi^2(x, y)$  are chosen such that their Fourier transforms satisfy

$$\sum_{m=-\infty}^{\infty} \sum_{i=1}^2 \hat{\psi}^i(2^m \omega_x, 2^m \omega_y) \hat{\chi}^i(2^m \omega_x, 2^m \omega_y) = 1,$$



the function  $s(x, y)$  may be reconstructed from its dyadic wavelet transform by

$$s(x, y) = \sum_{m=-\infty}^{\infty} \sum_{i=1}^2 W_m^i s * \chi_m^i(x, y),$$

where  $\chi_m^i(x, y) = 2^{-2m} \chi^i(2^{-m}x, 2^{-m}y)$ .

However, when processing discrete functions the scale  $2^m$  may no longer vary over all  $m \in \mathbf{Z}$ . Let the finest scale be normalized to 1 and the coarsest scale set to be  $2^M$ . Let us, similar to [11], introduce a real smoothing function  $\phi(x, y)$  such that its Fourier transform satisfies

$$|\hat{\phi}(\omega_x, \omega_y)|^2 = \sum_{m=0}^{\infty} \sum_{i=1}^2 \hat{\psi}^i(2^m \omega_x, 2^m \omega_y) \hat{\chi}^i(2^m \omega_x, 2^m \omega_y). \quad (26)$$

Here, as in one dimension, a finite energy discrete function ( $s(n_x, n_y) \in l^2(\mathbf{Z}^2)$ ) can be written as the uniform sampling of some function smoothed at scale 1:  $s(n_x, n_y) = S_0 f(n_x, n_y)$ , where  $f(x, y) \in L^2(\mathbf{R}^2)$  is not unique, and  $S_m f(x, y) = f * \phi_m(x, y)$ . This led Mallat and Zhong [11] to a two-dimensional analog of the one-dimensional definition of the discrete dyadic wavelet transform:<sup>5</sup>

$$\{S_{M-1} f(n_x + s, n_y + s), \{W_m^1 f(n_x + s, n_y + s), W_m^2 f(n_x + s, n_y + s)\}_{m \in [0, M-1]}\}_{(n_x, n_y) \in \mathbf{Z}^2}.$$

We will use, as in Section 2.2.2, a spline-based initialization procedure.

To implement a multidimensional discrete dyadic wavelet transform within a fast hierarchical digital filtering scheme, the wavelets were chosen to be separable products of one-dimensional functions:

$$\psi^1(x, y) = \psi(x) \phi(y), \quad (27)$$

$$\psi^2(x, y) = \psi(y) \phi(x), \quad (28)$$

where  $\phi(x)$  and  $\psi(x)$  were chosen as described in Section 2.2.2 (i.e.,  $\phi(x) = \beta_p(x)$  and  $\hat{\psi}(\omega)$  specified by (13)).

From (27), (28), and (13), we may write

$$\hat{\psi}^1(\omega_x, \omega_y) = G_{-s}(\omega_x) \hat{\beta}_p(\omega_x) \hat{\beta}_p(\omega_y), \quad (29)$$

$$\hat{\psi}^2(\omega_x, \omega_y) = G_{-s}(\omega_y) \hat{\beta}_p(\omega_x) \hat{\beta}_p(\omega_y), \quad (30)$$

where  $G(\omega)$  is given by (22) for  $d \in \{1, 2\}$ . Choosing

$$\hat{\chi}^1(\omega_x, \omega_y) = K_s(\omega_x) T_1(\omega_y) \hat{\beta}_p(\omega_x) \hat{\beta}_p(\omega_y), \quad (31)$$

$$\hat{\chi}^2(\omega_x, \omega_y) = K_s(\omega_y) T_1(\omega_x) \hat{\beta}_p(\omega_x) \hat{\beta}_p(\omega_y), \quad (32)$$

---

<sup>5</sup>As in Section 2.2.2, we put the finest scale of the transform at  $m = 0$ .

Table 5: Impulse responses  $t_1(n)$  for  $p \in \{0, 1, 2\}$ .

n	p=0	p=1	p=2
-3			0.0078125
-2		0.03125	0.046875
-1	0.125	0.125	0.1171875
0	0.75	0.6875	0.65625
1	0.125	0.125	0.1171875
2		0.03125	0.046875
3			0.0078125

where  $K(\omega)$  and  $T_1(\omega)$  are digital filter frequency responses, we may compute (26) for the finest two scales by

$$\sum_{i=1}^2 \hat{\psi}^i(2\omega_x, 2\omega_y) \hat{\chi}^i(2\omega_x, 2\omega_y) = |\hat{\phi}(\omega_x, \omega_y)|^2 - |\hat{\phi}(2\omega_x, 2\omega_y)|^2. \quad (33)$$

Inserting the terms defined by (29), (30), (31), (32), (12), and (16) with  $\hat{\phi}(\omega_x, \omega_y) = \hat{\beta}_p(\omega_x)\hat{\beta}_p(\omega_y)$  into (33) results in

$$K(\omega_x)G(\omega_x)T_1(\omega_y) + K(\omega_y)G(\omega_y)T_1(\omega_x) + |H(\omega_x)|^2|H(\omega_y)|^2 = 1. \quad (34)$$

Equation (34) represents a relation between the frequency responses of the digital filters used to implement a multidimensional discrete dyadic wavelet transform and is a multidimensional analog to (17).

Solving (34) for  $T_1(\omega)$  by substituting  $K(\omega)G(\omega)$  from (17) yields the closed formula [11]

$$T_1(\omega) = \frac{1}{2} (1 + |H(\omega)|^2) \quad (35)$$

In Table 5 we provide the filter coefficients for  $T_1(\omega)$  from (35) for  $p \in \{0, 1, 2\}$ . All other filters from (34) were already specified in Section 2.2.2.

As in the one-dimensional case, a two-dimensional discrete dyadic wavelet transform can be implemented as a fast hierarchical filtering scheme. To derive such an implementation, we, similar to the one-dimensional case from Section 2.2.2, use the definition of the two-dimensional dyadic wavelet transform (25) and require  $\hat{s}(\omega_x, \omega_y) = 0$  for  $|\omega_x| > \pi$  or  $|\omega_y| > \pi$ . Using Shannon's sampling theorem in two dimensions [38], (29), (30), and  $m=0$ , we get

$$W_0^1 s(x, y) = \int_{-\infty}^{\infty} \int_{-\infty}^{\infty} \sum_{i_x=-\infty}^{\infty} \sum_{i_y=-\infty}^{\infty} s(i_x, i_y) \text{sinc}(t_x - i_x) \text{sinc}(t_y - i_y) \cdot \sum_{m=-\infty}^{\infty} g_{-s}(m) \beta_p(x - t_x - m) \beta_p(y - t_y) dt_x dt_y$$

and

$$W_0^2 s(x, y) = \int_{-\infty}^{\infty} \int_{-\infty}^{\infty} \sum_{i_x=-\infty}^{\infty} \sum_{i_y=-\infty}^{\infty} s(i_x, i_y) \text{sinc}(t_x - i_x) \text{sinc}(t_y - i_y) \cdot \\ \cdot \beta_p(x - t_x) \sum_{m=-\infty}^{\infty} g_{-s}(m) \beta_p(y - t_y - m) dt_x dt_y.$$

As in one dimension, we make use of the fact that the cardinal spline functions converge to the sinc function as their order  $r$  tends to infinity, and write

$$\widehat{W}_0^1 s(\omega_x, \omega_y) \simeq S(\omega_x, \omega_y) B_r^{-1}(\omega_x) B_r^{-1}(\omega_y) \hat{\beta}_{p+r+1}(\omega_x) \hat{\beta}_{p+r+1}(\omega_y) G_{-s}(\omega_x)$$

and

$$\widehat{W}_0^2 s(\omega_x, \omega_y) \simeq S(\omega_x, \omega_y) B_r^{-1}(\omega_x) B_r^{-1}(\omega_y) \hat{\beta}_{p+r+1}(\omega_x) \hat{\beta}_{p+r+1}(\omega_y) G_{-s}(\omega_y),$$

or for  $m \in [0, M)$  and discrete signal processing

$$\mathcal{F}\{W_m^1 s(x, y) \big|_{x=n_x, y=n_y}\} \simeq S(\omega_x, \omega_y) B_r^{-1}(\omega_x) B_r^{-1}(\omega_y) B_{p+r+1}(\omega_x) \cdot \\ \cdot B_{p+r+1}(\omega_y) G_{-s}(2^m \omega_x) \prod_{i=0}^{m-1} H_{-s}(2^i \omega_x) H_{-s}(2^i \omega_y). \quad (36)$$

and

$$\mathcal{F}\{W_m^2 s(x, y) \big|_{x=n_x, y=n_y}\} \simeq S(\omega_x, \omega_y) B_r^{-1}(\omega_x) B_r^{-1}(\omega_y) B_{p+r+1}(\omega_x) \cdot \\ \cdot B_{p+r+1}(\omega_y) G_{-s}(2^m \omega_y) \prod_{i=0}^{m-1} H_{-s}(2^i \omega_x) H_{-s}(2^i \omega_y). \quad (37)$$

Equations (36) and (37) describe the decomposition part of the filter bank implementation of a two-dimensional discrete dyadic wavelet transform. The reconstruction part can be obtained from (31)–(33) with (12) and (16). The entire filter bank implementation of the transform is shown in Figure 9. Except for the prefiltering and postfiltering, we readily recognize the implementation proposed in [11].

Using the fact that a wavelet  $\psi(x)$  is equal to a first ( $d=1$ ) or a second ( $d=2$ ) derivative of a spline function  $\beta_{p+d}(x)$ , (27) and (28) may be rewritten as

$$\psi^i(x, y) = \frac{\partial^d \vartheta^i(x, y)}{\partial x_i^d}, \quad i, d \in \{1, 2\},$$

where

$$\vartheta^1(x, y) = \beta_{p+d}(x) \beta_p(y)$$

and

$$\vartheta^2(x, y) = \beta_p(x) \beta_{p+d}(y).$$

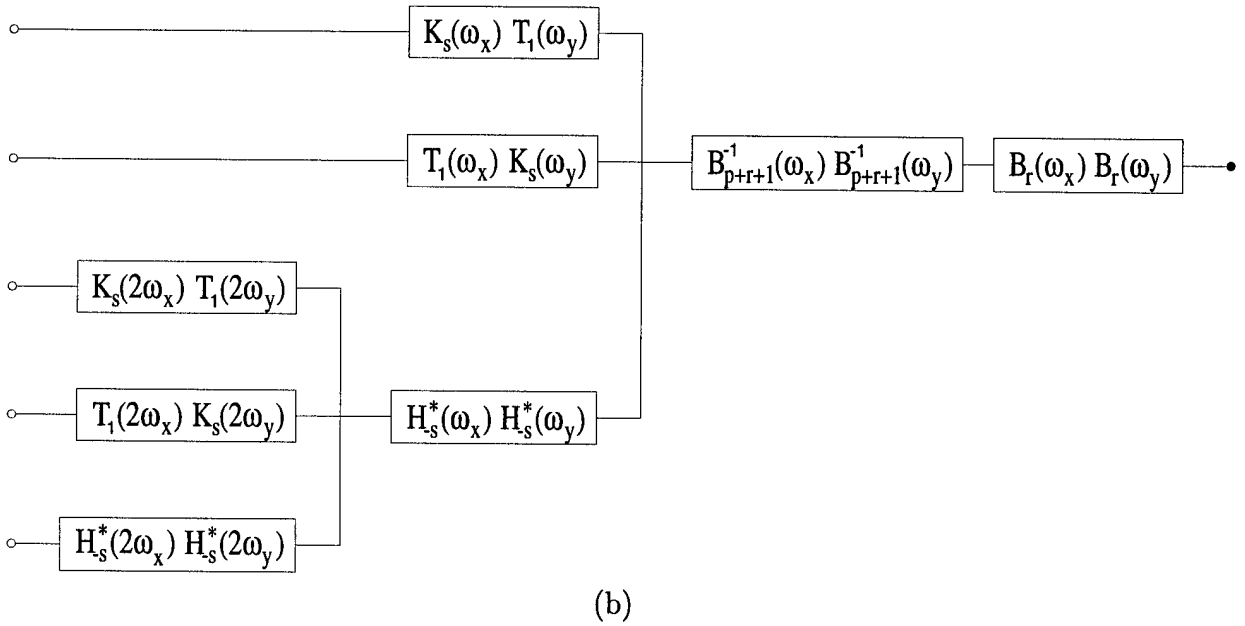
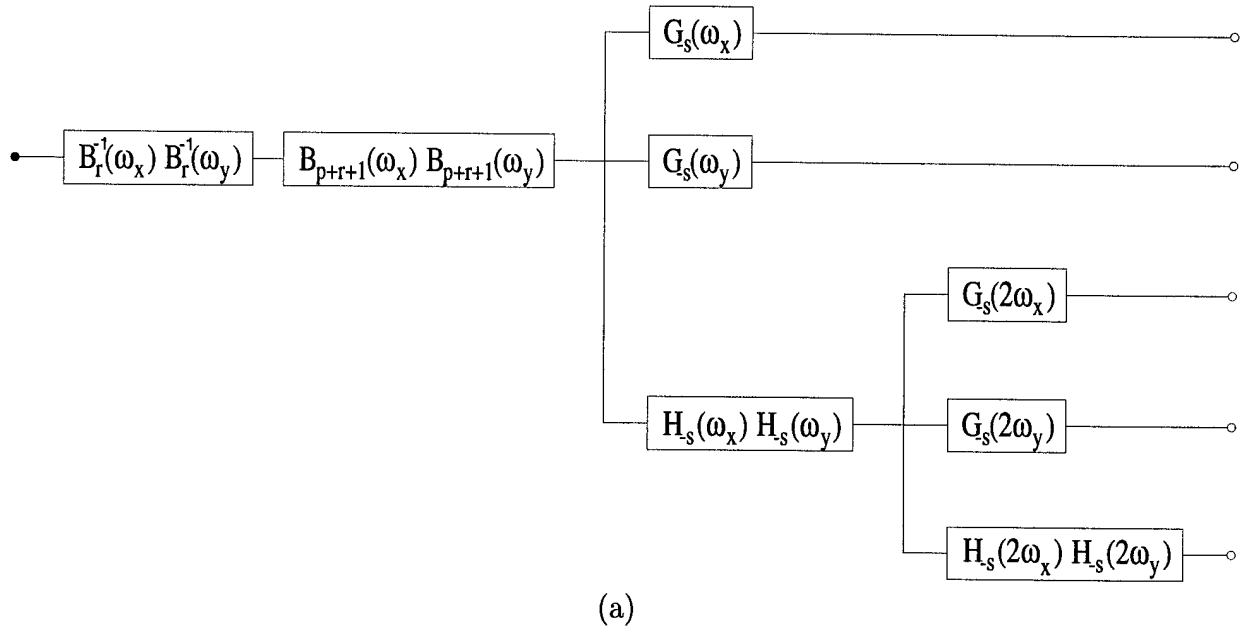


Figure 9: Filter bank implementation of a two-dimensional discrete dyadic wavelet transform (a) decomposition and (b) reconstruction for two levels of analysis.  $H_{-s}^*(\omega)$  denotes the complex conjugate of  $H_{-s}(\omega)$ .

Let us denote  $\vec{W}_m s(x, y) = (W_m^1 s(x, y), W_m^2 s(x, y))$ ,  $\vec{\nabla} = (\frac{\partial}{\partial x}, \frac{\partial}{\partial y})$ ,  $\Delta = \vec{\nabla}^2 = (\frac{\partial^2}{\partial x^2} + \frac{\partial^2}{\partial y^2})$ , and assume that  $\vartheta^i(x, y)$  can be approximated by  $\vartheta(x, y)$  for both  $i \in \{1, 2\}$ .

For  $d=1$  it then follows that

$$\vec{W}_m s(x, y) = 2^m \vec{\nabla} (s * \vartheta_m)(x, y). \quad (38)$$

Thus for  $d=2$  we can write

$$\sum_{i=1}^2 W_m^i s(x, y) = 2^{2m} \Delta (s * \vartheta_m)(x, y). \quad (39)$$

With  $\vartheta(x, y)$  being a Gaussian, finding local extrema of (38) in the direction of gradient  $\vec{\nabla}$  corresponds to the filtering stage of a Canny edge detector [33], and finding zero-crossings of (39) corresponds to the filtering carried out with a Marr-Hildreth edge detector (Laplacian of Gaussian) [39]. (Note that both edge detectors involve postprocessing). Edge detection based on finding local extrema of  $\vec{W}_m s(x, y)$  or zero-crossings of  $\sum_{i=1}^2 W_m^i s(x, y)$  is therefore an approximation to the Canny or the Marr-Hildreth edge detector over a range of dyadic scales. The differences stem from the fact that  $\vartheta(x, y)$  is neither a Gaussian nor is  $\vartheta^i(x, y)$  equal to  $\vartheta(x, y)$ .

### 2.2.5 Steerable Functions

When extending the transform from Section 2.2.2 to two dimensions, one of the first questions that come to mind is how to deal with the fact that derivatives can be defined in any direction of the plane.<sup>6</sup> In case of a first derivative of a Gaussian, one can simply compute first derivatives of a Gaussian in  $x$  and  $y$  directions and then determine the derivative in any direction from these two directional derivatives [33]. For higher order derivatives of a Gaussian, Freeman and Adelson [34] showed that order+1 directional operators are needed for synthesizing the operator at any orientation. In fact, functions with the property of expressing their arbitrary rotations as linear combinations of some functions are not limited to derivatives of a Gaussian. Below, we briefly restate some of the results from [34].

A two-dimensional function is called “steerable” if its rotations generate a finite dimensional space. Rotations of a steerable function  $f(r, \theta)$  can therefore be expressed as

$$f(r, \theta - \theta_0) = \sum_{i=1}^I c_i(\theta_0) f_i(r, \theta), \quad (40)$$

---

<sup>6</sup>Second derivatives of central B-splines can be used, as we saw in Section 2.2.4, to approximate Laplacian of a Gaussian for approximately rotation-invariant, although not directional, processing.

where  $\theta_0$  denotes an arbitrary angle,  $\{c_i(\theta_0)\}$  stands for a set of interpolating functions,  $\{f_i(r, \theta)\}$  is a set of basis functions, and  $r = \sqrt{x^2 + y^2}$  and  $\theta = \arg(x, y)$  are polar radius and angle, respectively.

If  $f(r, \theta)$  represents a filter kernel, the result of filtering with a rotated filter  $f(r, \theta - \theta_0)$  can be computed simply by  $\{c_i(\theta_0)\}$  weighted linear combination of outputs from basis filters  $\{f_i(r, \theta)\}$ . Only the outputs from basis filters need to be precomputed and then the output from a filter rotated by any angle  $\theta_0$  can be found by interpolating between them. When a large number of rotations of a template filter is required, the above scheme can lead to substantial savings in both computational cost (time) and memory requirements (space). The necessary condition for a function  $f(r, \theta)$  to be steerable is that  $f(r, \theta)$  is bandlimited in its polar angle:

$$f(r, \theta) = \sum_{n=-N}^N a_n(r) e^{jn\theta}. \quad (41)$$

This can be verified by inserting (41) into (40) and by assuming, for convenience, that  $f_i(r, \theta) = f(r, \theta - \theta_i)$ :

$$a_n(r) e^{-jn\theta_0} = \sum_{i=1}^I c_i(\theta_0) a_n(r) e^{-jn\theta_i}, \quad (42)$$

where  $\{\theta_i\}$  is a set of user defined angles and  $n \in [-N, 0]$ .<sup>7</sup> Since only nonzero coefficients  $a_n(r)$  are of interest, both sides of (42) can be divided by  $a_n(r)$ . This yields a matrix equation from which interpolating functions  $c_i(\theta_0)$  can be determined:

$$\begin{bmatrix} 1 \\ e^{j\theta_0} \\ \vdots \\ e^{jN\theta_0} \end{bmatrix} = \begin{bmatrix} 1 & 1 & \cdots & 1 \\ e^{j\theta_1} & e^{j\theta_2} & \cdots & e^{j\theta_I} \\ \vdots & \vdots & & \vdots \\ e^{jN\theta_1} & e^{jN\theta_2} & \cdots & e^{jN\theta_I} \end{bmatrix} \begin{bmatrix} c_1(\theta_0) \\ c_2(\theta_0) \\ \vdots \\ c_I(\theta_0) \end{bmatrix}. \quad (43)$$

For coefficients  $a_n = 0$  the rows corresponding to each  $n$  were removed from the matrix formulation shown in (43). For this system to have a solution, the angles  $\{\theta_i\}$  must be chosen such that the columns of the matrix are linearly independent.

In [34] they proved that the minimum number of basis functions  $f_i(r, \theta)$  needed to steer  $f(r, \theta)$  according to (40) is equal to the number of nonzero coefficients  $a_n(r)$  in the Fourier series expansion (41).

To conclude this brief description of steerability, let us only remark that functions which are not steerable (i.e., do not have a finite number of terms in (41)) can be approximated with steerable functions (a singular value decomposition was employed for approximating such functions efficiently [40]), and that the technique of expressing transformed versions of

---

<sup>7</sup>Note that the constraints are the same for  $n \in [-N, -1]$  and  $n \in [1, N]$ , so that a subset of all possible values for  $n \in [-N, N]$  can be taken.

a function as linear combinations of a fixed set of basis functions is not limited to rotations (extensions to translations [41], scalings [40, 41], and general transformations [42] have been reported).

### 2.2.6 Steerable Dyadic Wavelet Transform

Returning to the question from the beginning of Section 2.2.5, the answer seems obvious: one needs to construct a steerable analog to the one-dimensional transform from Section 2.2.2. Steerable transforms are nothing new—quite a few [43, 44, 45, 41] have been devised, some of them [44, 45] exactly for the computation of directional derivatives. Here, we are not interested in any directional derivatives: we want to use derivatives of central B-splines which, as the order of B-splines increases, tend to derivatives of a Gaussian.

We define a steerable dyadic wavelet transform of a function  $s(x, y) \in L^2(\mathbf{R}^2)$  at a scale  $2^m$ ,  $m \in \mathbf{Z}$ , as [9]

$$W_m^i s(x, y) = s * \psi_m^i(x, y), \quad (44)$$

where  $\psi_m^i(x, y)$  denotes  $\psi_m(x, y)$  rotated by  $\theta_i$ ,  $\psi_m(x, y) = 2^{-2m}\psi(2^{-m}x, 2^{-m}y)$ ,  $\psi(x, y)$  is a steerable wavelet that can be steered with I basis functions, and  $\theta_i = \frac{i-1}{I}\pi$  with  $i \in \{1, 2, \dots, I\}$ .

Analogously to the one-dimensional case (cf. Section 2.2.2) we require the two-dimensional Fourier plane to be covered by the dyadic dilations of  $\hat{\psi}^i(2^m\omega_x, 2^m\omega_y)$ : there must exist  $A_3 > 0$  and  $B_3 < \infty$  such that

$$A_3 \leq \sum_{m=-\infty}^{\infty} \sum_{i=1}^I |\hat{\psi}^i(2^m\omega_x, 2^m\omega_y)|^2 \leq B_3 \quad (45)$$

is satisfied almost everywhere.

If (nonunique) reconstructing functions  $\chi_m^i(x, y)$  are chosen such that their Fourier transforms satisfy

$$\sum_{m=-\infty}^{\infty} \sum_{i=1}^I \hat{\psi}^i(2^m\omega_x, 2^m\omega_y) \hat{\chi}^i(2^m\omega_x, 2^m\omega_y) = 1, \quad (46)$$

the function  $s(x, y)$  may be reconstructed from its steerable dyadic wavelet transform by

$$s(x, y) = \sum_{m=-\infty}^{\infty} \sum_{i=1}^I W_m^i s * \chi_m^i(x, y), \quad (47)$$

where  $\chi_m^i(x, y)$  denotes  $\chi_m(x, y)$  rotated by  $\theta_i$  and  $\chi_m(x, y) = 2^{-2m}\chi(2^{-m}x, 2^{-m}y)$ .

To derive an algorithm for the fast computation of the transform, we, similar to (10), introduce two smoothing functions such that

$$\hat{\phi}(\omega_x, \omega_y) \hat{\phi}(\omega_x, \omega_y) = \sum_{m=0}^{\infty} \sum_{i=1}^I \hat{\psi}^i(2^m\omega_x, 2^m\omega_y) \hat{\chi}^i(2^m\omega_x, 2^m\omega_y). \quad (48)$$

We choose wavelets that are steerable analogs to the one-dimensional wavelets from Section 2.2.2:<sup>8</sup>

$$\hat{\psi}(\omega_r, \omega_\theta) = (j\omega_r \cos(\omega_\theta))^d \left( \frac{\sin(\frac{\omega_r}{2})}{\frac{\omega_r}{2}} \right)^{p+d+1}, \quad (49)$$

where  $\omega_r = \sqrt{\omega_x^2 + \omega_y^2}$  and  $\omega_\theta = \arg(\omega_x, \omega_y)$ . These wavelets can be steered with  $d+1$  basis functions (i.e.,  $I$  in (40) is equal to  $d+1$ ).

Choosing

$$\hat{\phi}(2\omega_r) = H_{st}(\omega_r) \hat{\phi}(\omega_r), \quad (50)$$

$$\hat{\psi}^i(\omega_r, \omega_\theta) = G_{st}(\omega_r, \omega_\theta - \theta_i) \hat{\phi}(\omega_r), \quad (51)$$

$$\hat{\varphi}(2\omega_r) = L_{st}(\omega_r) \hat{\varphi}(\omega_r), \quad (52)$$

and

$$\hat{\chi}^i(\omega_r, \omega_\theta) = K_{st}(\omega_r, \omega_\theta - \theta_i) \hat{\varphi}(\omega_r), \quad (53)$$

and using (50) through (53) with (48) computed for the finest two scales, we obtain

$$\sum_{i=1}^I G_{st}(\omega_r, \omega_\theta - \theta_i) K_{st}(\omega_r, \omega_\theta - \theta_i) + H_{st}(\omega_r) L_{st}(\omega_r) = 1. \quad (54)$$

Setting  $\hat{\phi}(\omega_r) = \hat{\beta}_p(\omega_r)$ , and employing (12) and (49) with (50) and (51), we find that

$$H_{st}(\omega_r) = H_{-s}(\omega_r) \quad (55)$$

and

$$G_{st}(\omega_r, \omega_\theta) = (\cos(\omega_\theta))^d G_{-s}(\omega_r), \quad (56)$$

where  $H(\omega)$  and  $G(\omega)$  are specified by (16) and (22), respectively.

By inserting (55) and (56) into (54), the missing two filters can be chosen as

$$L_{st}(\omega_r) = L_s(\omega_r) \quad (57)$$

and

$$K_{st}(\omega_r, \omega_\theta) = \frac{1}{C_d} (\cos(\omega_\theta))^d K_s(\omega_r), \quad (58)$$

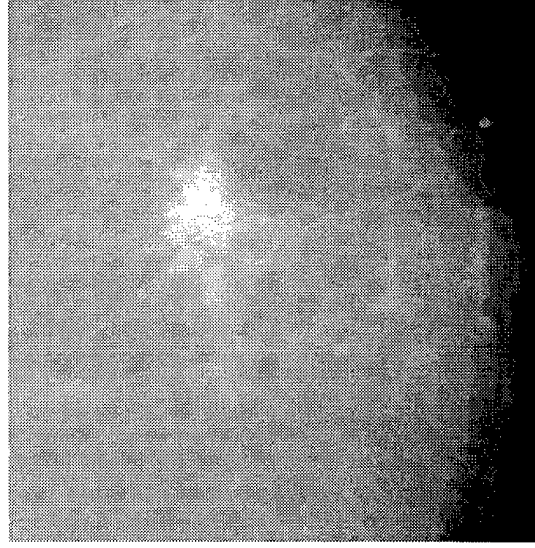
where  $L(\omega)$  and  $K(\omega)$  are given by (23) and (24), respectively, and  $C_d = \sum_{i=1}^I (\cos(\omega - \theta_i))^{2d}$ .

Figure 10 shows a mammogram and the corresponding wavelet transform coefficients for the second derivative ( $d=2$ ) wavelet. Wavelet transform coefficients for the fourth derivative ( $d=4$ ) wavelet are shown in Figure 11. With increasing order of the derivative, the orientation selectivity becomes better.

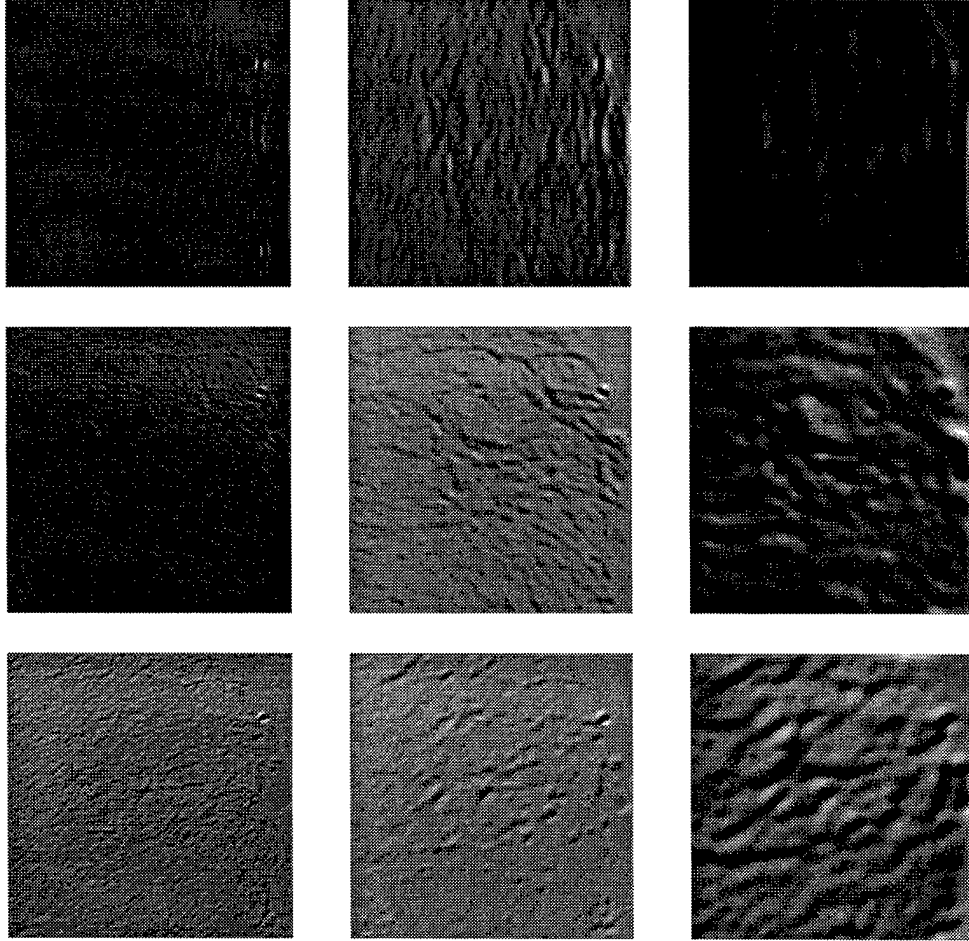
---

<sup>8</sup>This choice can be viewed as an extension of the transform presented in [46, 9, 47].





(a)



(b)

Figure 10: (a) Original mammogram. (b) Wavelet coefficients for  $d=2$ ,  $m \in \{2, 3, 4\}$  (left to right), and  $\theta_i = \frac{i-1}{3}\pi$ ,  $i \in \{1, 2, 3\}$  (top to bottom).

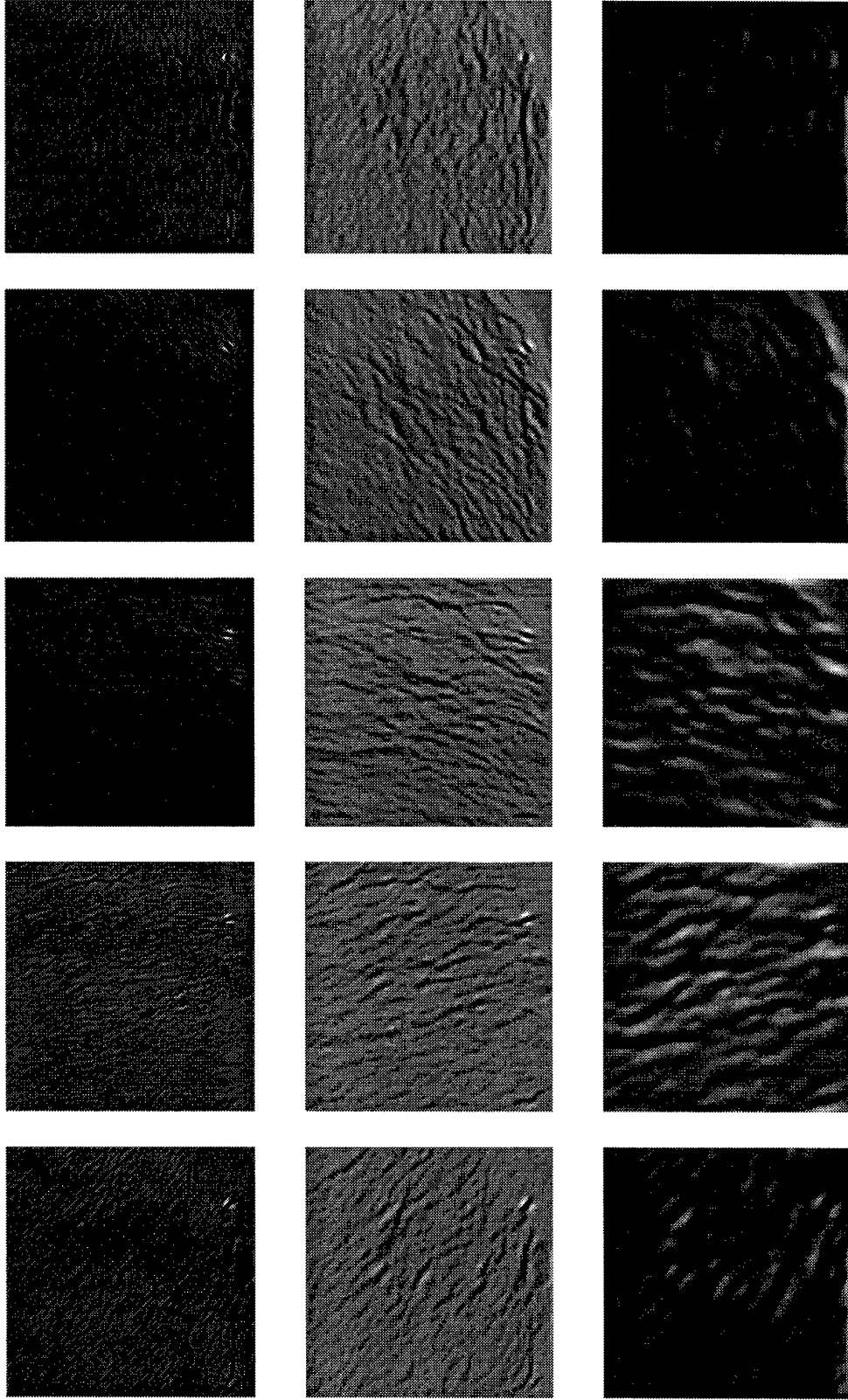


Figure 11: Wavelet coefficients for mammogram from Figure 10(a).  $d=4$ ,  $m \in \{2, 3, 4\}$  (left to right), and  $\theta_i = \frac{i-1}{5}\pi$ ,  $i \in \{1, 2, 3, 4, 5\}$  (top to bottom).

### 2.2.7 Multiscale Spline Derivative-Based Transform

Let us pause here for a brief assessment of the two-dimensional steerable transform derived so far. We have chosen steerable wavelets (49) which are equal to  $d$ -th order derivatives of circularly symmetric spline functions in the direction of  $x$ -axis (note that knots for these splines are circles) and we have laid a foundation for filter bank implementations in (54). An obvious shortcoming of this scheme is the fact that none of the filter kernels obtained from (55) through (58) is compactly supported on the rectangular grid. For implementations using digital filters, one is therefore forced to approximate these frequency responses, and by doing so, (54) may not hold anymore. Filters in filter bank implementations of steerable pyramids described in [44, 45, 41], for example, were designed by using various techniques for approximating desired frequency responses. None of the reported filter banks achieved perfect reconstruction and all filter kernels were nonseparable. Here, we will take a different approach. We will approximate the wavelets in (49) in a way that will lead to  $x$ - $y$  separable filters in a perfect reconstruction filter bank implementation of the transform such that the quality of approximation will improve by increasing the order of B-splines.

Let us approximate wavelets from (49) with

$$\psi(x, y) = \frac{d^d \beta_{p+d}(x)}{dx^d} \beta_{p+d}(y). \quad (59)$$

Based on the fact that B-splines tend to a Gaussian as their order increases, it is easy to see that both wavelets (49) and (59) converge to the same functions (i.e.,  $d$ -th order derivatives of the normalized Gaussian in the direction of  $x$ -axis) as  $p \rightarrow \infty$ .

In order to steer wavelets  $\psi(x, y)$  given by (59) (note that steering will be only approximate, since these wavelets are not steerable), we need to find basis functions that will approximately steer  $\psi(x, y)$ . Computing rotations, as we did in (44), is not practical here, because arbitrary rotations of (59) cannot be expressed exactly in terms of central B-spline functions from Section 2.1. Instead, we take advantage of the property of circularly symmetric functions that rotations of their directional derivatives are equal to directional derivatives in rotated directions:

$$\mathcal{R}_{\theta_0} \left\{ \frac{\partial^d \varrho_c(x, y)}{\partial \vec{n}^d} \right\} = \frac{\partial^d \varrho_c(x, y)}{\partial \vec{n}_{\theta_0}^d},$$

where  $\mathcal{R}_{\theta_0}$  stands for rotation by  $\theta_0$ ,  $\frac{\partial \varrho_c(x, y)}{\partial \vec{n}} = \vec{n} \cdot \vec{\nabla} \varrho_c(x, y)$ ,  $\varrho_c(x, y)$  is a circularly symmetric function, and  $\vec{n}_{\theta_0}$  denotes vector  $\vec{n} = (\cos \theta, \sin \theta)$  rotated by  $\theta_0$ .

Let us choose

$$\varrho(x, y) = \beta_{p+d}(x) \beta_{p+d}(y),$$

which is approximately circularly symmetric function for higher order splines. A rotation of  $\psi(x, y) = \frac{\partial^d \varrho(x, y)}{\partial x^d}$  from (59) by  $\theta_0$  can therefore be approximated by

$$\psi^{\theta_0}(x, y) \simeq \frac{\partial^d \varrho(x, y)}{\partial \vec{n}^d} = \sum_{i=0}^d \binom{d}{i} n_x^{d-i} n_y^i \frac{d^{d-i} \beta_{p+d}(x)}{dx^{d-i}} \frac{d^i \beta_{p+d}(y)}{dy^i}, \quad (60)$$

where  $\vec{n} = (\cos \theta_0, \sin \theta_0) = (n_x, n_y)$ .

Note that in case of Gaussian, which is both  $x$ - $y$  separable and circularly symmetric, (60) becomes exact (e.g., for  $\varrho(x, y) = e^{-(x^2+y^2)}$ ,  $\theta_0 = -\theta$ , and  $d = \{2, 4\}$ , we obtain, up to a scaling factor,  $x$ - $y$  separable basis set for the second and fourth derivative of Gaussian from Tables III and VII of [34]).

Having found a set of basis functions (60) that approximately steer wavelets (59), we want to construct a transform such that Equations (44) through (48) will be valid (superscript  $i$  must be viewed now as an index, rather than rotation by  $\theta_i$ ). In frequency domain, we can express basis functions from (60) as

$$\hat{\psi}^{i+1}(\omega_x, \omega_y) = G_{-s}^{d-i}(\omega_x) G_{-s}^i(\omega_y) \hat{\beta}_{p+i}(\omega_x) \hat{\beta}_{p+d-i}(\omega_y), \quad i = 0, 1, \dots, d, \quad (61)$$

where  $G^d(\omega)$  is given by (22) and  $G^0(\omega) = 1$ .

Choosing appropriate  $\hat{\chi}^i(\omega_x, \omega_y)$  to obtain a relation needed for the filter bank implementation of the transform is more complicated than in one dimension. Since we could not find a general solution for arbitrary  $d$ , we solve each case separately. Below, we present solutions for the first four orders. When  $d \leq 2$ , we impose  $\hat{\varphi}(\omega_x, \omega_y) = \hat{\phi}(\omega_x, \omega_y) = \hat{\beta}_p(\omega_x) \hat{\beta}_p(\omega_y)$ , a constraint analogous to the one from Section 2.2.2. For  $d = 1$ , we write similar to [11]

$$\hat{\chi}^1(\omega_x, \omega_y) = K_s^1(\omega_x) T_1(\omega_y) \hat{\beta}_p(\omega_x) \hat{\beta}_{p-1}(\omega_y), \quad (62)$$

$$\hat{\chi}^2(\omega_x, \omega_y) = T_1(\omega_x) K_s^1(\omega_y) \hat{\beta}_{p-1}(\omega_x) \hat{\beta}_p(\omega_y), \quad (63)$$

where  $K^d(\omega)$  and  $T_1(\omega)$  are given by (24) and (35), respectively.

Computing (48) for the finest two scales and inserting (12), (61), (62), and (63) yields a relation between frequency responses

$$G^1(\omega_x) K^1(\omega_x) T_1(\omega_y) + T_1(\omega_x) G^1(\omega_y) K^1(\omega_y) + |H(\omega_x) H(\omega_y)|^2 = 1.$$

For  $d = 2$ , we choose

$$\hat{\chi}^1(\omega_x, \omega_y) = K_s^2(\omega_x) T_2(\omega_y) \hat{\beta}_p(\omega_x) \hat{\beta}_{p-2}(\omega_y), \quad (64)$$

$$\hat{\chi}^2(\omega_x, \omega_y) = K_s^1(\omega_x) K_s^1(\omega_y) \hat{\beta}_{p-1}(\omega_x) \hat{\beta}_{p-1}(\omega_y), \quad (65)$$

$$\hat{\chi}^3(\omega_x, \omega_y) = T_2(\omega_x) K_s^2(\omega_y) \hat{\beta}_{p-2}(\omega_x) \hat{\beta}_p(\omega_y), \quad (66)$$

where

$$T_2(\omega) = |H(\omega)|^2. \quad (67)$$

Using (12), (61), and (64) through (66) with (48) results in

$$G^2(\omega_x)K^2(\omega_x)T_2(\omega_y) + G^1(\omega_x)K^1(\omega_x)G^1(\omega_y)K^1(\omega_y) + T_2(\omega_x)G^2(\omega_y)K^2(\omega_y) + |H(\omega_x)H(\omega_y)|^2 = 1.$$

For orders  $d > 2$ , we require  $\hat{\phi}(\omega_x, \omega_y) = \hat{\beta}_p(\omega_x)\hat{\beta}_p(\omega_y)$  and  $\hat{\phi}(\omega_x, \omega_y) = \hat{\phi}(\omega_x)\hat{\phi}(\omega_y)$ , where  $\hat{\phi}(\omega)$  is specified by (14) and (23).

For  $d = 3$ , we choose reconstructing functions

$$\hat{\chi}^1(\omega_x, \omega_y) = K_s^3(\omega_x)\hat{\phi}(\omega_x)\hat{\phi}_{-3}(\omega_y), \quad (68)$$

$$\hat{\chi}^2(\omega_x, \omega_y) = -K_s^2(\omega_x)K_s^1(\omega_y)V_3(\omega_x)V_3(\omega_y)\hat{\phi}_{-1}(\omega_x)\hat{\phi}_{-2}(\omega_y), \quad (69)$$

$$\hat{\chi}^3(\omega_x, \omega_y) = -K_s^1(\omega_x)K_s^2(\omega_y)V_3(\omega_x)V_3(\omega_y)\hat{\phi}_{-2}(\omega_x)\hat{\phi}_{-1}(\omega_y), \quad (70)$$

$$\hat{\chi}^4(\omega_x, \omega_y) = K_s^3(\omega_y)\hat{\phi}_{-3}(\omega_x)\hat{\phi}(\omega_y), \quad (71)$$

where

$$V_3(\omega) = \frac{1}{\sqrt{2}}(1 - |H(\omega)|^2), \quad (72)$$

and  $\hat{\phi}_{-i}(\omega) \in L^1(\mathbf{R})$  denotes a function such that  $\hat{\phi}(\omega) = \hat{\beta}_{i-1}(\omega)\hat{\phi}_{-i}(\omega)$ ,  $i \in \mathbf{N}$ .

Employing (61), (12), (14), and (68) through (71) with (48) yields a relation

$$G^3(\omega_x)K^3(\omega_x) - G^2(\omega_x)K^2(\omega_x)V_3(\omega_x)G^1(\omega_y)K^1(\omega_y)V_3(\omega_y) - G^1(\omega_x)K^1(\omega_x)V_3(\omega_x)G^2(\omega_y)K^2(\omega_y)V_3(\omega_y) + G^3(\omega_y)K^3(\omega_y) + H(\omega_x)L(\omega_x)H(\omega_y)L(\omega_y) = 1,$$

where  $L(\omega)$  is specified by (23).

For  $d = 4$ , our choices are

$$\hat{\chi}^1(\omega_x, \omega_y) = K_s^4(\omega_x)T_2(\omega_y)\hat{\phi}(\omega_x)\hat{\phi}_{-4}(\omega_y), \quad (73)$$

$$\hat{\chi}^2(\omega_x, \omega_y) = K_s^3(\omega_x)K_s^1(\omega_y)\hat{\phi}_{-1}(\omega_x)\hat{\phi}_{-3}(\omega_y), \quad (74)$$

$$\hat{\chi}^3(\omega_x, \omega_y) = -K_s^2(\omega_x)K_s^2(\omega_y)V_4(\omega_x)V_4(\omega_y)\hat{\phi}_{-2}(\omega_x)\hat{\phi}_{-2}(\omega_y), \quad (75)$$

$$\hat{\chi}^4(\omega_x, \omega_y) = K_s^1(\omega_x)K_s^3(\omega_y)\hat{\phi}_{-3}(\omega_x)\hat{\phi}_{-1}(\omega_y), \quad (76)$$

$$\hat{\chi}^5(\omega_x, \omega_y) = T_2(\omega_x)K_s^4(\omega_y)\hat{\phi}_{-4}(\omega_x)\hat{\phi}(\omega_y), \quad (77)$$

where

$$V_4(\omega_x) = 1 - |H(\omega)|^2. \quad (78)$$

Using the above functions (73) through (77), (61), (12), and (14) in (48) computed for the finest two scales gives

$$\begin{aligned} & G^4(\omega_x)K^4(\omega_x)T_2(\omega_y) + G^3(\omega_x)K^3(\omega_x)G^1(\omega_y)K^1(\omega_y) - \\ & -G^2(\omega_x)K^2(\omega_x)V_4(\omega_x)G^2(\omega_y)K^2(\omega_y)V_4(\omega_y) + G^1(\omega_x)K^1(\omega_x)G^3(\omega_y)K^3(\omega_y) + \\ & +T_2(\omega_x)G^4(\omega_y)K^4(\omega_y) + H(\omega_x)L(\omega_x)H(\omega_y)L(\omega_y) = 1. \end{aligned}$$

Here, we have even more freedom for choosing the reconstructing functions than in one dimension. The above functions for  $d = \{2, 3, 4\}$  were found by trying to imitate the one-dimensional transform from Section 2.2.2 as much as possible. All decomposition filters  $G^d(\omega)$  were first paired with corresponding reconstruction filters  $K^d(\omega)$ , and then all other potential digital filters were specified as polynomials in  $H_{-s}(\omega)$ . We inserted thus specified filters into a relation between their frequency responses and solved for the unknown polynomial coefficients. Since we allowed more filters with higher-degree polynomials than expected in the solution, the resulting system of linear equations was underdetermined. This allowed enough freedom for removal of undesired digital filters and for balance between degrees of polynomials.

The described procedure for determination of reconstructing functions and filters involves quite a lot of heuristics to obtain the appropriate solution from the underdetermined linear system. Unfortunately, we are not aware of any systematic way (aside from numerical optimization, which may be pretty cumbersome) to obtain solutions comparable to the ones above.

Next, we will derive a filter bank implementation of the transform. As in Section 2.2.4, we assume a bandlimited input signal:  $\hat{s}(\omega_x, \omega_y) = 0$  for  $|\omega_x| > \pi$  or  $|\omega_y| > \pi$ . Using Shannon's sampling theorem in two dimensions [38] with (44) and basis functions from (61), we can write

$$\begin{aligned} W_0^i s(x, y) &= \int_{-\infty}^{\infty} \int_{-\infty}^{\infty} \sum_{i_x=-\infty}^{\infty} \sum_{i_y=-\infty}^{\infty} s(i_x, i_y) \text{sinc}(t_x - i_x) \text{sinc}(t_y - i_y) \cdot \\ &\cdot \sum_{m_x=-\infty}^{\infty} g_{-s}^{d-i}(m_x) \beta_{p+i}(x - t_x - m_x) \sum_{m_y=-\infty}^{\infty} g_{-s}^i(m_y) \beta_{p+d-i}(y - t_y - m_y) dt_x dt_y, \end{aligned}$$

where  $i = 0, 1, \dots, d$  as in (61).

Again, we approximate sinc functions with  $r$ -order cardinal splines, then use (4), and get

$$\begin{aligned} \text{DFT}\{W_m^i s(x, y) \big|_{x=n_x, y=n_y}\} &\simeq S(\omega_x, \omega_y) B_r^{-1}(\omega_x) B_r^{-1}(\omega_y) B_{p+r+i+1}(\omega_x) \cdot \\ &\cdot B_{p+r+d-i+1}(\omega_y) G_{-s}^{d-i}(2^m \omega_x) G_{-s}^i(2^m \omega_y) \prod_{n=0}^{m-1} H_{-s}^{p+i}(2^n \omega_x) H_{-s}^{p+d-i}(2^n \omega_y). \end{aligned} \quad (79)$$

Using (79) with an approximation  $B_{p+r+i+1}(\omega) \simeq B_{p+r}(\omega)B_i(\omega)$ , we can obtain a filter bank implementation of the transform decomposition. The reconstruction part follows from (48), (61), and reconstructing functions for distinct values of  $d$ . Figure 12 shows filter bank implementations of a multiscale spline derivative-based transform for  $d = \{1, 2, 3, 4\}$ . For  $d = 1$ , we recognize (except for the prefiltering and postfiltering) the filter bank implementation of a two-dimensional discrete dyadic wavelet transform from [11]. For  $d = 2$ , however, our transform differs from the filter bank presented in [8] (i.e., the corresponding transform described in Section 2.2.4): second derivative is computed only in the directions of  $x$  and  $y$ -axis in [12, 8], which is not enough for steering. Although not particularly appropriate for orientation analysis, such a scheme may still, as we have seen in Section 2.2.4, efficiently approximate Laplacian of Gaussian across dyadic scales. A transform similar to the one described in this section, was presented in [44, 45, 41]. Their filter bank implementation is less redundant (downsampling is used on the lowpass branch, while simultaneously keeping aliasing negligible by using a filter with insignificant amount of energy for  $|\omega_r| > \frac{\pi}{2}$ ) and uses reconstruction filters with same magnitude frequency responses as the decomposition ones—a possible advantage for certain applications. They have, on the other hand, little control over the function from which derivatives are computed (to obtain a  $d$ -th derivative, they multiply a circularly symmetric filter by  $(-j \cos \theta)^d$  with all filters being obtained by recursive minimization of a weighted combination of constraints), filter bank does not have perfect reconstruction, and none of the filters is  $x$ - $y$  separable.

## 2.2.8 Finite Impulse Response Filters

Since all two-dimensional filters used in the filter bank implementations of the transforms from previous sections are  $x$ - $y$  separable, we will begin this section with a detailed description of FIR filter implementations for the one-dimensional discrete dyadic wavelet transform implementation from Figure 6. The extension to two dimensions will then be straightforward.

Let us refer to filters applied at scale  $2^m$  as filters at level  $m+1$ , and let filters at level 1 (Equations (16), (22) through (24), (35), (67), (72), and (78)) be called “original filters,” to distinguish them from their upsampled versions. As an input to the filter bank from Figure 6, we consider a real signal  $s(n) \in l^2(\mathbf{Z})$ ,  $n \in [0, N-1]$ . Depending on the length of each filter impulse response, filtering an input signal may be computed either by multiplying the discrete Fourier transforms of the two sequences or by circularly convolving  $s(n)$  with a filter’s impulse response.<sup>9</sup> Of course, such a periodically extended signal may change

---

<sup>9</sup>As is customary in image processing, we use circular, rather than linear, convolution.

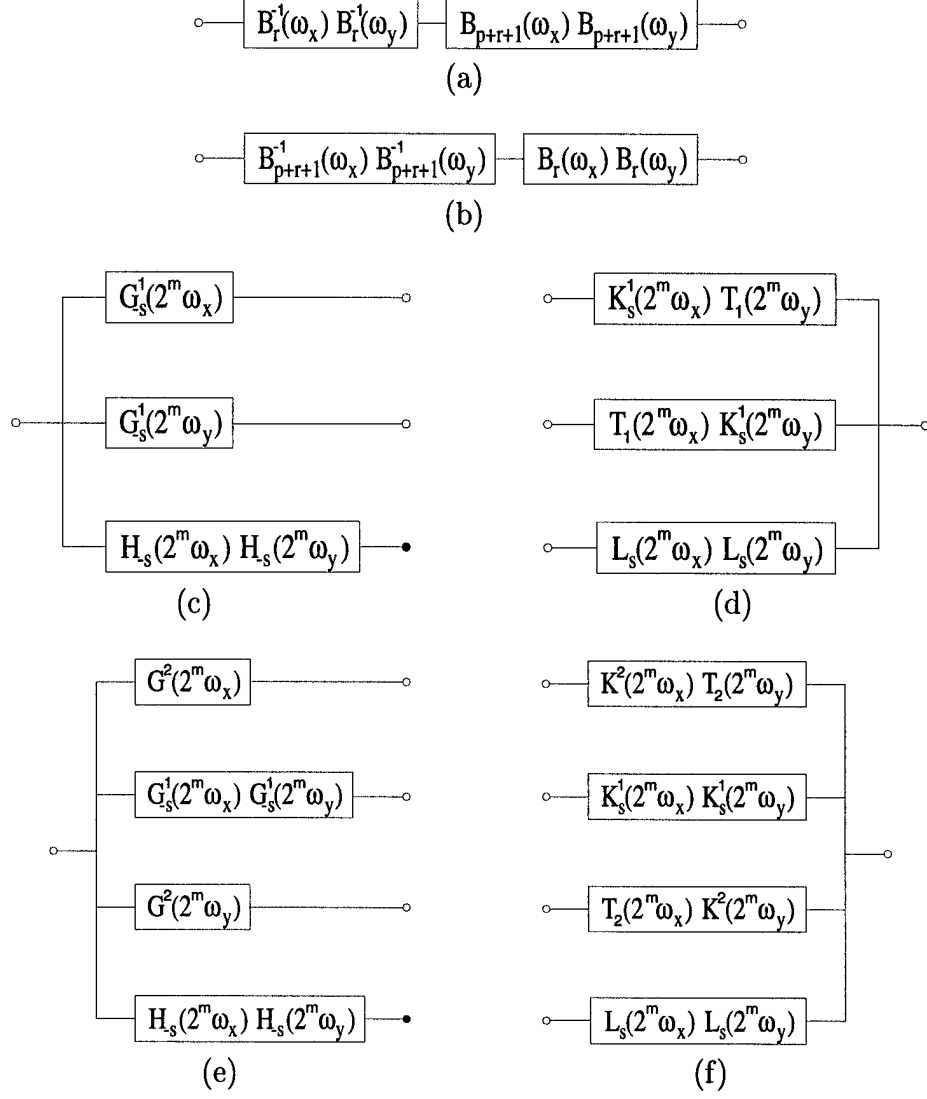


Figure 12: Filter bank implementation of a multiscale spline derivative-based transform for  $m \in [0, M - 1]$ : (a) Prefiltering, (b) postfiltering, (c) decomposition and (d) reconstruction modules for  $d = 1$ , and (e) decomposition and (f) reconstruction modules for  $d = 2$ .



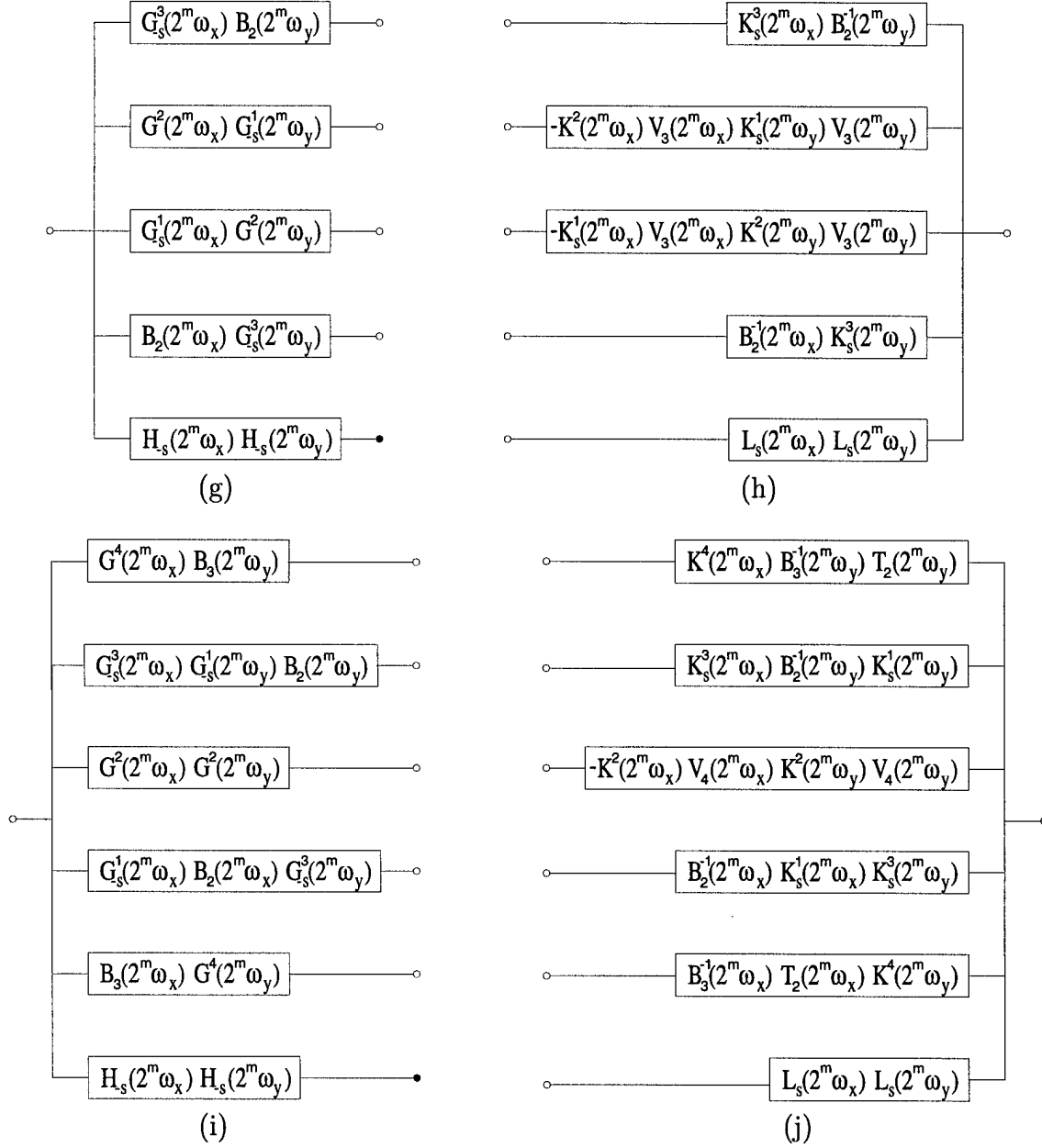


Figure 12: Continued: (g) Decomposition and (h) reconstruction modules for  $d = 3$ , and (i) decomposition and (j) reconstruction modules for  $d = 4$ . Decomposition modules are recursively applied at the locations of the filled circles.

abruptly at the boundaries causing artifacts. A common remedy for such a problem is realized by constructing a mirror extended signal [12]

$$s_{me}(n) = \begin{cases} s(-n-1) & \text{if } n \in [-N, -1] \\ s(n) & \text{if } n \in [0, N-1], \end{cases} \quad (80)$$

where we chose the signal  $s_{me}(n)$  to be supported in  $[-N, N-1]$ . It will become evident shortly, that mirror extension is particularly elegant in conjunction with symmetric/antisymmetric filters.

Let us first classify symmetric/antisymmetric real even-length signals into four types [23]:

$$\text{Type I } f(n) = f(-n),$$

$$\text{Type II } f(n) = f(-n-1),$$

$$\text{Type III } f(n) = -f(-n),$$

$$\text{Type IV } f(n) = -f(-n-1),$$

where  $n \in [-N, N-1]$ . Note that for Type I signals the values at  $f(0)$  and  $f(-N)$  are unique, and that for Type III signals the values at  $f(0)$  and  $f(-N)$  are equal to zero.

Using properties of the Fourier transform it is easy to show that the convolution of symmetric/antisymmetric real signals results in a symmetric/antisymmetric real signal. If a symmetric/antisymmetric real signal has an even length, then there always exists an integer shift such that the shifted signal belongs to one of the above types.

Now, we are ready to examine the filter bank implementation of a one-dimensional discrete dyadic wavelet transform from Figure 6 with filters given by (16) and (22) through (24) driven by a mirrored signal  $s_{me}(n)$  at the input. Let the number of levels  $M$  be restricted by

$$M \leq 1 + \log_2 \frac{N-1}{L_{max}-1}, \quad (81)$$

where  $L_{max}$  is the length of the longest original FIR filter impulse response.

Each FIR filter block in the filter bank consists of a filter and a circular shift operator.

Equation (81) guarantees that the length of the filter impulse response does not exceed the length of the signal at any block.

Since our input signal  $s_{me}(n)$  is of Type II and noninteger shifts at level 1 are rounded to the nearest integer, it follows that a processed signal at any point in the filter bank belongs to one of the types defined above. This means that filtering a signal of length  $2N$  can be reduced to filtering a signal of approximately one half of its length. (For Types I and III,  $N+1$  samples are needed. However, for Type III one needs to store only  $N-1$  values because zero values are always present at the zeroth and  $(-N)$ -th sample position).

Implementation is particularly simple for FIR filters designed with  $d$  even and  $p$  odd. Filters are of Type I in this case, so the signal at any point of the filter bank will be of Type II. An FIR filter block from the filter bank shown in Figure 6 can therefore be implemented by

$$F_{s,m}u(n) = f(0)u_{II}(n) + \sum_{i=1}^{\frac{L-1}{2}} f(i)[u_{II}(n - 2^m i) + u_{II}(n + 2^m i)], \quad n \in [0, N - 1], \quad (82)$$

where

$$u_{II}(n) = \begin{cases} u(-n - 1) & \text{if } n \in [-\frac{N}{2}, -1] \\ u(n) & \text{if } n \in [0, N - 1] \\ u(2N - n - 1) & \text{if } n \in [N, \frac{3N}{2}], \end{cases} \quad (83)$$

$u(n)$  is an input signal to a block,  $f(n)$  is an impulse response of some original filter,  $L$  is the length of the filter, and  $N$  is the length of an input signal  $s(n)$  to the filter bank. Implementation of filters  $b_p(n)$  used for prefiltering and postfiltering represents a special case of (82) with  $m=0$ .

A filter bank with the above implementation of blocks and signal  $s(n)$  at the input yields equivalent results as circular convolution for  $s_{me}(n)$  as defined by (80). In addition to requiring one half the amount of memory, the computational savings over a circular convolution implementation of blocks are, depending on the original filter length, three to four times fewer multiplications and one half as many additions.

A similar approach can be used for other filters. However, things get slightly more complicated in this case, because the filters are not of the same type and the signal components within the filter bank are of distinct types. As a consequence, an implementation of blocks that use distinct original filters may not be the same, and the implementation of blocks at level 1 may differ from the implementation of blocks at other levels of analysis.

The decomposition blocks at level 1 can be implemented by

$$G_{-s,0}u(n) = \sum_{i=0}^{\frac{L}{2}-1} g(i)[u_{II}(n - i - 1) - u_{II}(n + i)], \quad n \in [1, N - 1],$$

for  $d$  odd, (82) for  $d$  even,

$$H_{-s,0}u(n) = \sum_{i=0}^{\frac{L}{2}-1} h(i)[u_{II}(n - i - 1) + u_{II}(n + i)], \quad n \in [0, N],$$

for  $p$  even, and (82) for  $p$  odd, where  $u_{II}(l)$  is defined by (83),  $g(n)$  and  $h(n)$  are impulse responses of the filters computed from (22) and (16), respectively, and  $L$  is the length of the corresponding impulse response.

The output from a block  $G_{-s}(\omega)$  at level 1 is of Type III for  $d$  odd and of Type II for  $d$  even, while the output from  $H_{-s}(\omega)$  at the same level is of Type I for  $p$  even and of Type II for  $p$  odd.

The decomposition blocks at subsequent levels  $m \in [1, M-1]$  can be implemented by

$$G_{-s,m}u(n) = \sum_{i=0}^{\frac{L}{2}-1} g(i)[u_I(n - 2^m(i+s)) - u_I(n + 2^m(i+s))], \quad n \in [1, N-1],$$

for  $d$  odd and  $p$  even,

$$G_{-s,m}u(n) = \sum_{i=0}^{\frac{L}{2}-1} g(i)[u_{II}(n - 2^m(i+s)) - u_{II}(n + 2^m(i+s))], \quad n \in [0, N-1],$$

for  $d$  and  $p$  odd,

$$F_{-s,m}u(n) = f(0)u_I(n) + \sum_{i=1}^{\frac{L-1}{2}} f(i)[u_I(n - 2^m i) + u_I(n + 2^m i)], \quad n \in [0, N], \quad (84)$$

with  $f(n) = g(n)$  for  $d$  and  $p$  even,

$$H_{-s,m}u(n) = \sum_{i=0}^{\frac{L}{2}-1} h(i)[u_I(n - 2^m(i+s)) + u_I(n + 2^m(i+s))], \quad n \in [0, N], \quad (85)$$

for  $p$  even, and (82) for  $p$  odd, where

$$u_I(n) = \begin{cases} u(-n) & \text{if } n \in [-\frac{N}{2}, -1] \\ u(n) & \text{if } n \in [0, N] \\ u(2N - n) & \text{if } n \in [N+1, \frac{3N}{2}]. \end{cases} \quad (86)$$

The outputs from blocks  $G_{-s}(2^m\omega)$  are of Type III for  $d$  odd and  $p$  even, of Type IV for  $d$  and  $p$  odd, and of Type I for  $d$  and  $p$  even, whereas the outputs from  $H_{-s}(2^m\omega)$  are of Type I for  $p$  even and of Type II for  $p$  odd.

Next, the reconstruction blocks at level 1 can be implemented by

$$K_{s,0}u(n) = \sum_{i=1}^{\frac{L}{2}} k(i)[u_{III}(n - i + 1) - u_{III}(n + i)], \quad n \in [0, N-1],$$

for  $d$  odd, (82) for  $d$  even,

$$L_{s,0}u(n) = \sum_{i=1}^{\frac{L}{2}} l(i)[u_I(n - i + 1) + u_I(n + i)], \quad n \in [0, N-1],$$

for  $p$  even, and (82) for  $p$  odd, where

$$u_{III}(n) = \begin{cases} -u(-n) & \text{if } n \in [-\frac{N}{2}, -1] \\ 0 & \text{if } n = 0 \\ u(n) & \text{if } n \in [1, N-1] \\ 0 & \text{if } n = N \\ -u(2N - n) & \text{if } n \in [N+1, \frac{3N}{2}], \end{cases} \quad (87)$$

$u_I(n)$  is as defined by (86) and  $k(n)$  is an impulse response of the filter from (24). Note that both outputs from blocks  $K_s(\omega)$  and  $L_s(\omega)$  are of Type II.

The reconstruction blocks at subsequent levels can be implemented by

$$K_{s,m}u(n) = \sum_{i=0}^{\frac{L}{2}-1} k(i+1)[u_{III}(n - 2^m(i+s)) - u_{III}(n + 2^m(i+s))], \quad n \in [0, N],$$

for  $d$  odd and  $p$  even, (84) with  $f(n) = k(n)$  for  $d$  and  $p$  even,

$$K_{s,m}u(n) = \sum_{i=0}^{\frac{L}{2}-1} k(i+1)[u_{IV}(n - 2^m(i+s)) - u_{IV}(n + 2^m(i+s))], \quad n \in [0, N-1],$$

for  $d$  and  $p$  odd,

$$L_{s,m}u(n) = H_{-s,m}u(n),$$

for  $p$  even, and (82) for  $p$  odd, where  $u_{III}(l)$  is given by (87),

$$u_{IV}(n) = \begin{cases} -u(-n-1) & \text{if } n \in [-\frac{N}{2}, -1] \\ u(n) & \text{if } n \in [0, N-1] \\ -u(2N-n-1) & \text{if } n \in [N, \frac{3N}{2}], \end{cases}$$

and  $H_{-s,m}u(n)$  is specified by (85). We observe that the outputs from blocks  $K_s(2^m\omega)$  and  $L_s(2^m\omega)$ ,  $m \in [1, M-1]$ , are of Type I for  $p$  even, and of Type II for  $p$  odd.

When we compare the above implementation of blocks to circular convolution driven by a mirrored signal  $s_{me}(n)$  at the input, we observe that approximately twofold less memory space, three to four times fewer multiplications and one half as many additions are required. (For Type I signals an additional sample has to be saved because two values are without a pair).

Until now, we have talked only about the one-dimensional case, whose filter bank implementation is depicted in Figure 12. Two-dimensional transform filter bank implementations (Figures 9 and 12) are not only comprised of  $x$ - $y$  separable filters solely, but also use all the filters from Section 2.2.2. Everything presented in this section so far is therefore directly applicable to the two-dimensional case. Filters which have not been treated yet (i.e.,  $t_1(n)$ ,  $t_2(n)$ ,  $v_3(n)$ ,  $v_4(n)$ , and filters  $b_p(n)$  from the decomposition modules of Figure 12) can all be realized by (82) for  $p$  odd or  $m = 0$  and (84) otherwise ( $f(n)$  denotes an impulse response of any of the above mentioned zero-phase filters in this case).<sup>10</sup> The implementation presented in this section performs all operations in the spatial domain, however, one could also implement the structures shown in Figures 6, 9, and 12 with an input signal  $s_{me}(n)$  (Equation (80)) in the frequency domain. For short filter impulse

<sup>10</sup>In case of filters  $v_3(n)$  and  $v_4(n)$ , a slightly more efficient implementation can be obtained by precomputing new filters  $k * v_3(n)$  and  $k * v_4(n)$ , and then implementing them by  $K_{s,m}u(n)$ ,  $m \in [0, M-1]$ .

responses, such as those given in Tables 2, 3 and 4, the spatial implementation described in this section is certainly more efficient. For long filter impulse responses, however, filtering is faster if implemented in the frequency domain. Additional details on alternative implementation strategies can be found in [48].

### 2.2.9 Infinite Impulse Response Filters

Implementation of IIR filters  $b_p^{-1}(n)$  which were introduced in Section 2.1.2 is a bit more involved than the one encountered in the previous section. Fortunately, the number of different cases is much smaller here: possible input to  $b_p^{-1}(n)$  in filter banks from Figures 6, 9, and 12 is either of Type II or of Type I.<sup>11</sup> We will use ideas and a few results from [20]. Let us first take a closer look at the system function  $B_p^{-1}(z)$ . This function can be written as a cascade of terms

$$E(z) = \frac{1}{z - \frac{1+\alpha^2}{\alpha} + z^{-1}} = \frac{-\alpha}{(1 - \alpha z^{-1})(1 - \alpha z)}, \quad (88)$$

which can be expressed in a parallel form as

$$E(z) = \frac{-\alpha}{1 - \alpha^2} \left( \frac{1}{1 - \alpha z^{-1}} + \frac{1}{1 - \alpha z} - 1 \right), \quad (89)$$

where  $\alpha$  and  $\frac{1}{\alpha}$  are poles of the causal and the anticausal filter, respectively.

The impulse response of this term can be written as

$$e(n) = \frac{-\alpha}{1 - \alpha^2} \alpha^{|n|}.$$

We choose to implement  $E(z)$  in a cascade form and therefore extract the difference equations from (88):

$$c^+(n) = u(n) + \alpha c^+(n-1) \quad n = 1, 2, \dots, N-1, \quad (90)$$

and

$$c(n) = \alpha (c(n+1) - c^+(n)) \quad n = N-2, N-3, \dots, 0, \quad (91)$$

where  $u(n)$  denotes the input to the block,  $c^+(n)$  is the output from the causal part, and  $c(n)$  stands for the output from the block.

To solve (90) and (91) we need boundary conditions  $c^+(0)$  and  $c(N-1)$ . Let us begin with filters  $b_p^{-1}(n)$  in filter bank implementations from Figures 6, 9, 12(a), 12(b), and Figures 12(h) and 12(j) with  $m=0$ . We derive

$$c^+(0) = \sum_{i=-\infty}^0 \alpha^{-i} u_{IIp}(i) = u(0) + \sum_{i=0}^{N-1} \frac{\alpha^{i+1} + \alpha^{2N-i}}{1 - \alpha^{2N}} u(i) \simeq u(0) + \sum_{i=0}^{i_0} \alpha^{i+1} u(i), \quad (92)$$

---

<sup>11</sup>Note that symmetry types in this section slightly differ from those defined in Section 2.2.8: here, mirror extended signals are periodically repeated, so that they stretch from  $-\infty$  to  $\infty$ .

and, using parallel form (89)

$$\begin{aligned} c(N-1) &= \frac{-\alpha}{1-\alpha^2} (c^+(N-1) + \sum_{i=0}^{N-1} \frac{\alpha^{N-i} + \alpha^{N+1+i}}{1-\alpha^{2N}} u(i)) \simeq \\ &\simeq \frac{-\alpha}{1-\alpha^2} (c^+(N-1) + \sum_{i=N-1-i_0}^{N-1} \alpha^{N-i} u(i)), \end{aligned} \quad (93)$$

where

$$\begin{aligned} u_{IIp}(n) &= \begin{cases} u_{II}(n \bmod (2N)) & \text{if } n \geq 0 \\ u_{II}(-(n+1) \bmod (2N)) & \text{if } n < 0, \end{cases} \\ u_{II}(n) &= \begin{cases} u(n) & \text{if } n \in [0, N-1] \\ u(2N-n-1) & \text{if } n \in [N, 2N-1], \end{cases} \end{aligned}$$

$N$  is the length of an input signal to the filter bank, and  $i_0 < N-1$  is selected such that  $\alpha^{i_0}$  falls below a predefined precision threshold.

For IIR filters from Figures 12(h) and 12(j) with  $m \in [1, M-1]$  and  $p$  odd, we get

$$\begin{aligned} c^+(0) &= \sum_{i=-\infty}^0 \left[ \alpha^{-\frac{i}{2^m}} u_{IIp}(i) \right]_u = \\ &= u(0) + \sum_{n=0}^{\infty} \sum_{i=0}^{N-1} \left\{ \left[ \alpha^{\frac{i+1+2Nn}{2^m}} \right]_u + \left[ \alpha^{\frac{2N(n+1)-i}{2^m}} \right]_u \right\} u(i) \end{aligned} \quad (94)$$

and

$$c(N-1) = \frac{-\alpha}{1-\alpha^2} (c^+(N-1) + \sum_{n=0}^{\infty} \sum_{i=0}^{N-1} \left\{ \left[ \alpha^{\frac{N-i+2Nn}{2^m}} \right]_u + \left[ \alpha^{\frac{N+1+i+2Nn}{2^m}} \right]_u \right\} u(i), \quad (95)$$

where

$$[\alpha^x]_u = \begin{cases} \alpha^x & \text{if } x \in \mathbf{Z} \\ 0 & \text{otherwise.} \end{cases}$$

If  $N$  is a power of two and  $2^{m-1} \leq N$  ((81) guarantees that the latter condition is always true) (94) becomes

$$c^+(0) = u(0) + \sum_{i=0}^{N-1} \frac{\left[ \alpha^{\frac{i+1}{2^m}} \right]_u + \left[ \alpha^{\frac{2N-i}{2^m}} \right]_u}{1 - \alpha^{\frac{2N}{2^m}}} u(i),$$

while (95) can be written as

$$c(N-1) = \frac{-\alpha}{1-\alpha^2} (c^+(N-1) + \sum_{i=0}^{N-1} \frac{\left[ \alpha^{\frac{N-i}{2^m}} \right]_u + \left[ \alpha^{\frac{N+1+i}{2^m}} \right]_u}{1 - \alpha^{\frac{2N}{2^m}}} u(i).$$

Finally, the boundary conditions for filters  $b_p^{-1}(n)$  from Figures 12(h) and 12(j) with  $m \in [1, M-1]$  and  $p$  even are

$$c^+(0) = \sum_{i=-\infty}^0 \left[ \alpha^{-\frac{i}{2^m}} u_{Ip}(i) \right]_u =$$

$$\begin{aligned}
&= \sum_{n=0}^{\infty} \left\{ \left[ \alpha^{\frac{2Nn}{2^m}} \right]_u u(0) + \left[ \alpha^{\frac{N(2n+1)}{2^m}} \right]_u u(N) + \right. \\
&\quad \left. + \sum_{i=1}^{N-1} \left\{ \left[ \alpha^{\frac{i+2Nn}{2^m}} \right]_u + \left[ \alpha^{\frac{2N(n+1)-i}{2^m}} \right]_u \right\} u(i) \right\}
\end{aligned} \tag{96}$$

and

$$c(N) = \frac{-\alpha}{1 - \alpha^2} (2c^+(N) - u(N)),$$

where

$$\begin{aligned}
u_{Ip}(n) &= u_I(|n| \bmod (2N)), \\
u_I(n) &= \begin{cases} u(n) & \text{if } n \in [0, N] \\ u(2N - n) & \text{if } n \in [N + 1, 2N - 1], \end{cases}
\end{aligned}$$

and  $c^-(N) = c^+(N)$  with  $c^-(n)$  denoting response of the anticausal filter from (89) was used.

Again, if  $N$  is a power of two and  $2^{m-1} \leq N$ , (96) can be simplified

$$c^+(0) = \frac{u(0) + \alpha^{\frac{N}{2^m}} u(N) + \sum_{i=1}^{N-1} \left\{ \left[ \alpha^{\frac{i}{2^m}} \right]_u + \left[ \alpha^{\frac{2N-i}{2^m}} \right]_u \right\} u(i)}{1 - \alpha^{\frac{2N}{2^m}}}.$$

Series in expressions for  $c^+(0)$ ,  $c(N-1)$ , and  $c(N)$  for filters from Figures 12(h) and 12(j) with  $m \in [1, M-1]$  can be, similar to (92) and (93), truncated according to the desired precision.

For orders  $p$  greater than three, we implement  $B_p^{-1}(z)$  as a cascade of terms  $E(z)$  with different  $\alpha$ 's. Note that the output from block  $E(z)$  is always of the same type as the input to it.

## 2.3 Image Fusion

Image fusion combines particular aspects of information from the same imaging modality or from distinct imaging modalities and can be used to improve the reliability of a particular computational vision task or to provide a human observer with a deeper insight about the nature of observed data. Whether it is combining different sensors or extending the dynamic range of a single sensor, the goal is to achieve more accurate inferences that can be achieved by a single sensor or a single sensor setting. By fusing together processed sections of images, a combined image which is superior to the sum of its parts can be constructed. We are developing methods by which transformed mammograms can be broken apart and fused together in a manner which will increase the overall mammogram interpretability. The simplest method of fusing images is accomplished by computing their average. Such a technique does combine features from input images in the fused image, however, the



contrast of the original features can be significantly reduced. Among more sophisticated methods, multiscale and multiresolution analyses have become particularly popular. Different pyramids [49, 50] and wavelet-based techniques [51, 46, 52, 53] have been applied to this problem.

In this section, we compare an image fusion method based upon the steerable dyadic wavelet transform with recently published fusion methods based upon the gradient pyramid, the orthogonal wavelet transform, and the biorthogonal wavelet transform. Sections 2.3.1 and 2.3.2 introduce the gradient pyramid and the discrete wavelet transform, respectively. For a more thorough treatment of these transforms, please refer to references cited therein. In Section 2.3.3, we examine the performance of all four transforms on examples with relation to mammography.

### 2.3.1 Gradient Pyramid

Gaussian pyramid [30] was used for construction of a gradient pyramid used in [49]. Let the generating filter kernel for the Gaussian pyramid be

$$w(n_x, n_y) = w_b * w_b(n_x, n_y) = \frac{1}{256} \begin{bmatrix} 1 & 4 & 6 & 4 & 1 \\ 4 & 16 & 24 & 16 & 4 \\ 6 & 24 & 36 & 24 & 6 \\ 4 & 16 & 24 & 16 & 4 \\ 1 & 4 & 6 & 4 & 1 \end{bmatrix},$$

where  $w_b(n_x, n_y)$  denotes the 3 by 3 binomial filter:

$$w_b(n_x, n_y) = \frac{1}{16} \begin{bmatrix} 1 & 2 & 1 \\ 2 & 4 & 2 \\ 1 & 2 & 1 \end{bmatrix}.$$

Level  $m \in \mathbf{N}$  of the Gaussian pyramid for an input image matrix  $s(n_x, n_y)$  is then

$$\mathcal{G}_m s(n_x, n_y) = (w * \mathcal{G}_{m-1} s(n_x, n_y))_{\downarrow 2},$$

with

$$\mathcal{G}_0 s(n_x, n_y) = s(n_x, n_y).$$

Gradient pyramid is obtained from the Gaussian pyramid as

$$\mathcal{D}_m^i s(n_x, n_y) = d_i * (\mathcal{G}_m s(n_x, n_y) + w_b * \mathcal{G}_m s(n_x, n_y)),$$

where

$$d_1 = \begin{bmatrix} 1 & -1 \end{bmatrix},$$

$$\begin{aligned}
d_2 &= \frac{1}{\sqrt{2}} \begin{bmatrix} 0 & -1 \\ 1 & 0 \end{bmatrix}, \\
d_3 &= \begin{bmatrix} -1 \\ 1 \end{bmatrix}, \text{ and} \\
d_4 &= \frac{1}{\sqrt{2}} \begin{bmatrix} -1 & 0 \\ 0 & 1 \end{bmatrix}.
\end{aligned}$$

An image is reconstructed from the gradient pyramid by converting the pyramid to the Laplacian and then to the Gaussian pyramid. The Laplacian pyramid is approximated as

$$\widehat{\mathcal{L}}_m s(n_x, n_y) \simeq \mathcal{K}_m s(n_x, n_y) + w * \mathcal{K}_m s(n_x, n_y), \quad (97)$$

where

$$\mathcal{K}_m s(n_x, n_y) = -\frac{1}{8} \sum_{i=1}^4 d_i * \mathcal{D}_m^i s(n_x, n_y).$$

An approximation to the Gaussian pyramid is obtained by

$$\widehat{\mathcal{G}}_m s(n_x, n_y) = \widehat{\mathcal{L}}_m s(n_x, n_y) + 4w * (\widehat{\mathcal{G}}_{m+1} s(n_x, n_y))_{\uparrow 2}.$$

Note that, since the filters  $d_i$  have the center of symmetry between samples, they need to be shifted for reconstruction, and that, because of the approximation (97), the gradient pyramid does not have the perfect reconstruction property.

### 2.3.2 Discrete Wavelet Transform

Discrete wavelet transform was implemented as a perfect reconstruction filter bank [54]. In two dimensions, the transform is obtained by applying the one-dimensional transform separately along each dimension. Level  $m \in \mathbf{N}$  of the transformed image matrix  $s(n_x, n_y)$  is therefore

$$\begin{aligned}
\mathcal{W}_m^d s(n_x, n_y) &= ((\mathcal{A}_{m-1} s(n_x, n_y) * \tilde{g}(n_x))_{\downarrow 2} * \tilde{g}(n_y))_{\downarrow 2}, \\
\mathcal{W}_m^v s(n_x, n_y) &= ((\mathcal{A}_{m-1} s(n_x, n_y) * \tilde{g}(n_x))_{\downarrow 2} * \tilde{h}(n_y))_{\downarrow 2}, \\
\mathcal{W}_m^h s(n_x, n_y) &= ((\mathcal{A}_{m-1} s(n_x, n_y) * \tilde{h}(n_x))_{\downarrow 2} * \tilde{g}(n_y))_{\downarrow 2}, \text{ and} \\
\mathcal{A}_m s(n_x, n_y) &= ((\mathcal{A}_{m-1} s(n_x, n_y) * \tilde{h}(n_x))_{\downarrow 2} * \tilde{h}(n_y))_{\downarrow 2},
\end{aligned}$$

where

$$\mathcal{A}_0 s(n_x, n_y) = s(n_x, n_y), \quad (98)$$

$\{\mathcal{W}_m^d s(n_x, n_y), \mathcal{W}_m^v s(n_x, n_y), \mathcal{W}_m^h s(n_x, n_y)\}_{m \in [1, M]}$  and  $\mathcal{A}_M s(n_x, n_y)$  are detail and approximation coefficients for  $M$  levels of analysis, respectively, and  $\tilde{g}(n)$  and  $\tilde{h}(n)$  are the decomposition filters.

Reconstruction of the approximation coefficients at the previous level is given by

$$\begin{aligned}\mathcal{A}_{m-1}s(n_x, n_y) = & ((\mathcal{W}_m^d s(n_x, n_y))_{\uparrow 2} * \bar{g}(n_y) + (\mathcal{W}_m^v s(n_x, n_y))_{\uparrow 2} * \bar{h}(n_y))_{\uparrow 2} * \bar{g}(n_x) + \\ & + ((\mathcal{W}_m^h s(n_x, n_y))_{\uparrow 2} * \bar{g}(n_y) + (\mathcal{A}_m s(n_x, n_y))_{\uparrow 2} * \bar{h}(n_y))_{\uparrow 2} * \bar{h}(n_x),\end{aligned}$$

with  $\bar{g}(n)$  and  $\bar{h}(n)$  being the reconstruction filters.

Two-dimensional wavelets associated with separable filter banks, such as the one just described, were constructed from tensor products of two one-dimensional multiresolution analyses (wavelets are products of one-dimensional wavelets and scaling functions) [17]. Note also that, due to oversimplified initialization (98), the discrete wavelet transform may be a pretty poor approximation to samples of the continuous wavelet transform.

We will limit ourselves to FIR filters (i.e., compactly supported wavelets). In our experiments, we will use orthogonal wavelet transform with DAUB12 wavelet [17], and biorthogonal wavelet transform with Bior6.8 wavelet from MATLAB Wavelet Toolbox.

### 2.3.3 Comparison of Transforms

Image fusion is performed in the transform space by computing local statistics across the decomposition scales, and reconstructing from fused transform coefficients. Typical size of neighborhood is between a single pixel and 5 by 5 area with some loss of contrast reported for the latter [49]. In general, the chosen size of the area represents a tradeoff between sharpness and introduction of artifacts. In order to achieve our goal of maximum contrast with minimum artifacts, we limit the neighborhood to a single pixel (maximizing contrast) and try to choose the most appropriate transform (minimizing artifacts).

After the transform decompositions of images to be fused is performed, the corresponding transform coefficients of the images are combined according to the fusion rule into a new set of transform coefficients from which the fused result is reconstructed. As a fusion rule, we used the maximum magnitude rule (at each position and scale of the transforms the coefficient with greatest magnitude is chosen) for the gradient pyramid, the orthogonal wavelet transform (DAUB12), and the biorthogonal wavelet transform (Bior6.8), and the maximum oriented energy rule (at each position and scale of the transforms the coefficient with greatest local oriented energy is selected) for steerable wavelet transform [46].

Our first two experiments used the phantom shown in Figure 13. Image matrix has dimensions 512 by 512, and fusion was performed between the original and shifted phantom.

First, the image to be fused with the one from Figure 13 was generated by shifting the phantom one sample vertically towards the top of the image. The ideal result of fusion should contain no double lines or other artifacts (the distance between the corresponding

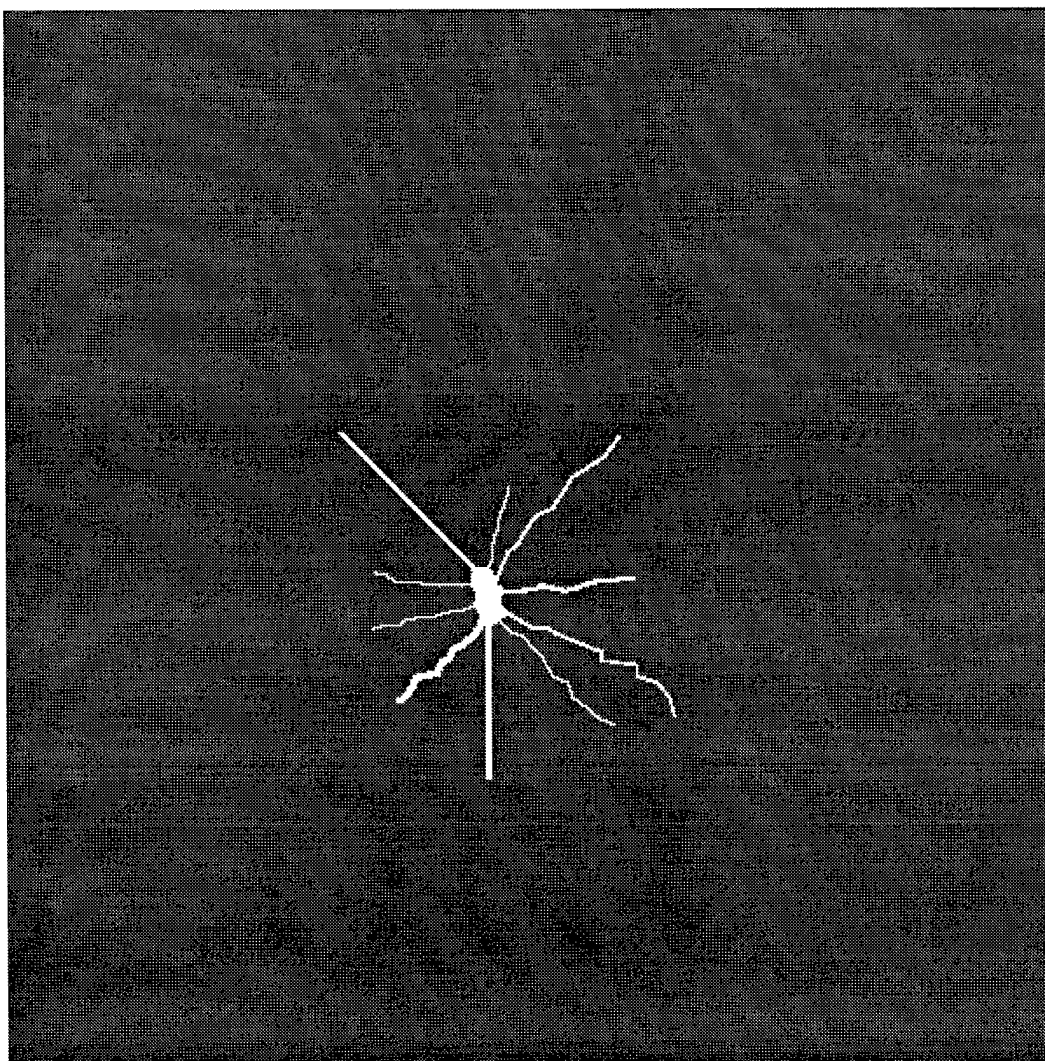


Figure 13: Phantom used for comparisons of different transforms for image fusion.

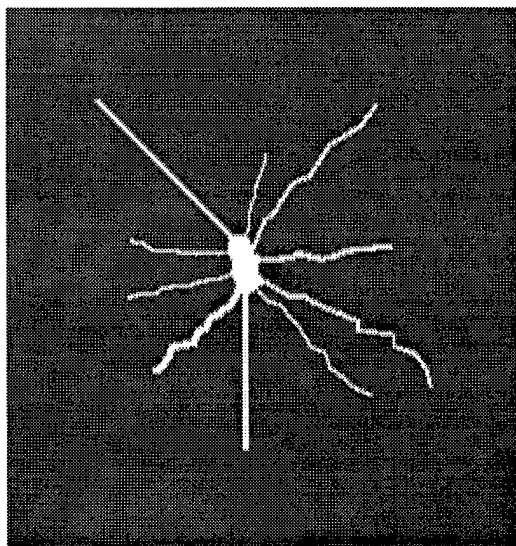
Table 6: Performance of fusion algorithms based on four different transforms.

Transform	MSE	MAE
Gradient pyramid	28.66	13
Orthogonal WT	0.14	8
Biorthogonal WT	0.21	7
Steerable WT	0.05	6

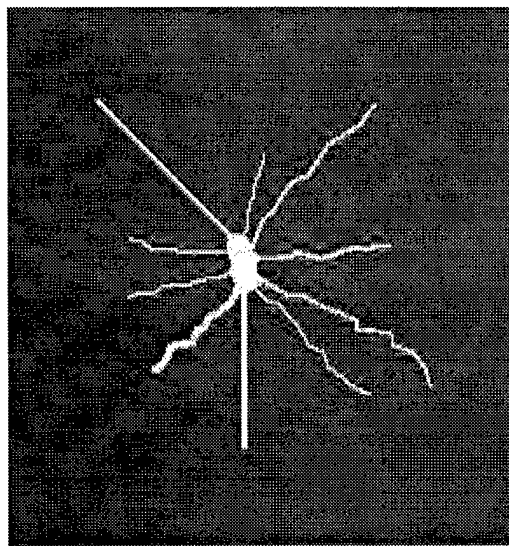
points in two images is one pixel, so that the algorithm should merge shifted features into a single feature). Figure 14 shows the phantom with the surrounding area in the fused images. The resulting images from all four transforms were clipped (pixel values above the upper limit of the gray level range were mapped to white) rather than scaled. Please note the artifacts present when the orthogonal and biorthogonal wavelet transforms were used. The latter produced a slightly better result, although artifacts due to aliasing and tensor product representation made both fused images unacceptable.

Our second experiment differed from the first one only in the fact that the phantom from Figure 13 was shifted by five samples. Here, the shift is large enough that features from both images may be present in the fused image. The phantom with its surroundings in the results of fusion using the four transforms is demonstrated in Figure 15. Please note that the situation is similar to the one in the first experiment. Both orthogonal and biorthogonal wavelet transforms exhibited obvious artifacts, while the redundant gradient pyramid and steerable dyadic wavelet transform performed well.

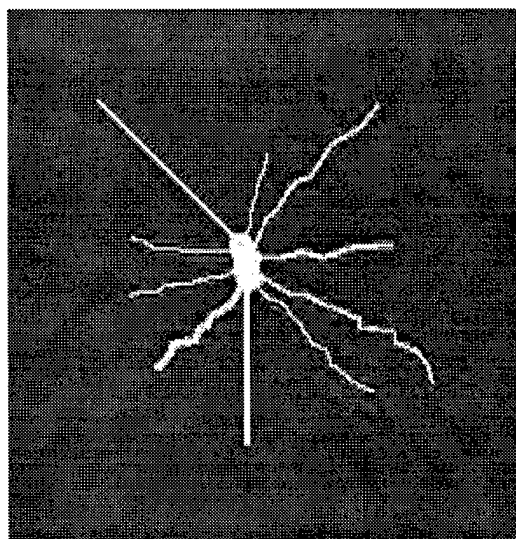
The third experiment was geared towards a quantitative comparison of the four transforms for image fusion. Similar to [52], we blur different parts of the image and then fuse them in such a way that each blurred part is fused with its original counterpart. The ideal result of fusion would be the original image. Figure 16 shows the original 512 by 512 mammogram, 100 by 100 area of interest, and two blurred images to be fused. Mean-square error (MSE) and maximum absolute error (MAE) between the result of fusion and the original image were computed for all four methods. Table 6 summarizes the results. Let us remark that these results are rather typical; on a variety of images, wavelet based methods were very close, while consistently outperforming the gradient pyramid according to the two criteria. No significant artifacts were noticed in the “blurring experiments.” By comparing the extracted regions with the original ones, we subjectively rated the transforms used for fusion as: (1) steerable dyadic wavelet transform, (2) biorthogonal wavelet transform, (3) orthogonal wavelet transform, and (4) gradient pyramid. Again, the differences between different types of wavelet transforms were minor, whereas the gradient pyramid lagged behind. Regions of interest corresponding to the one from Figure 16(b) are shown in Figure 17. Wavelet based methods produced results that are visually close to the original region,



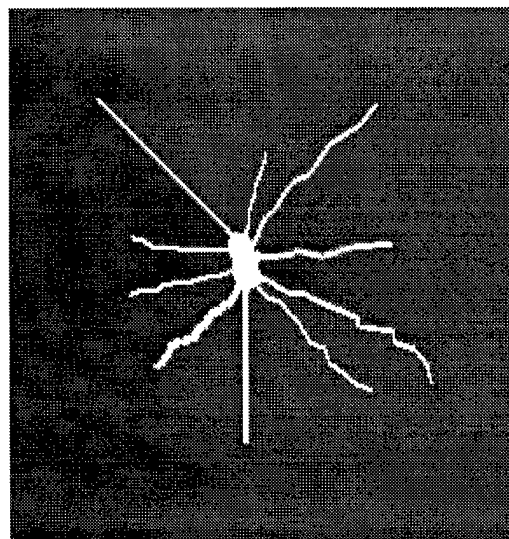
(a)



(b)

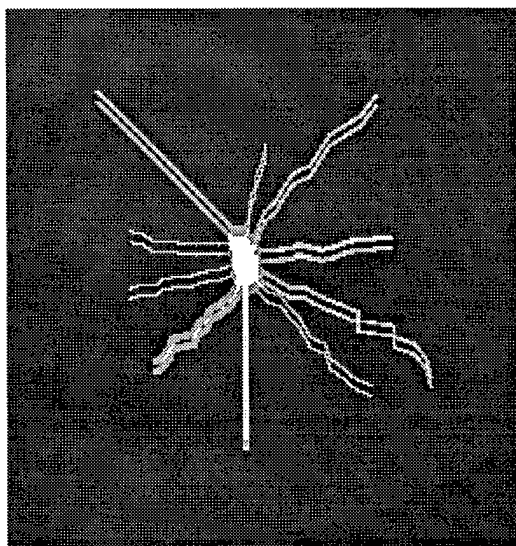


(c)

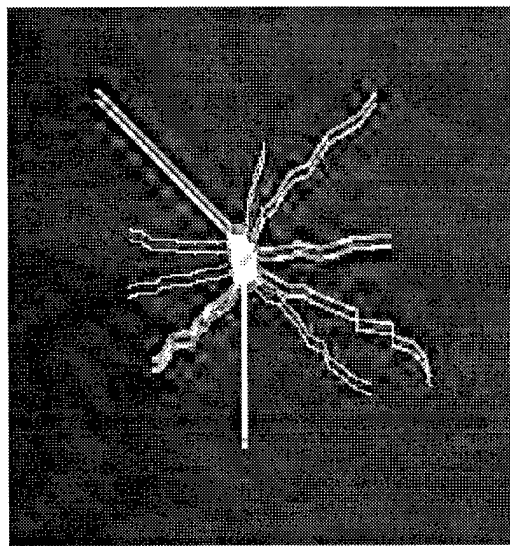


(d)

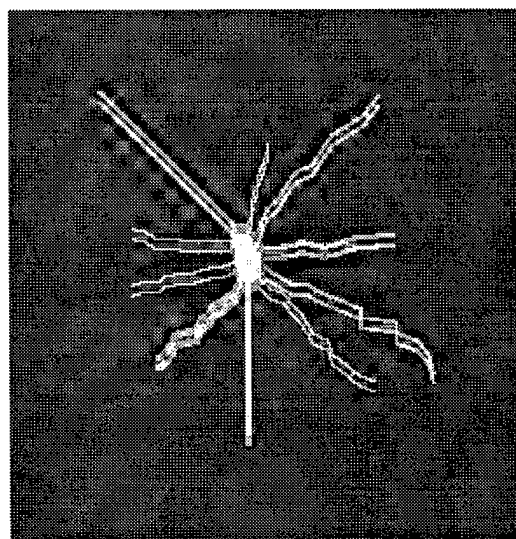
Figure 14: Image fusion of phantoms shifted by one sample. (a) Gradient pyramid. (b) Orthogonal wavelet transform. (c) Biorthogonal wavelet transform. (d) Steerable dyadic wavelet transform.



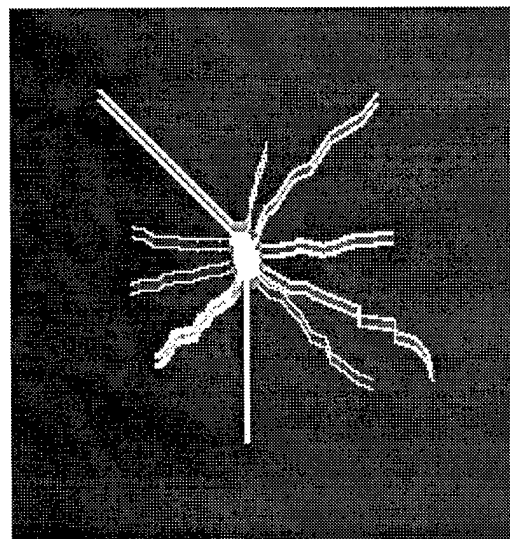
(a)



(b)

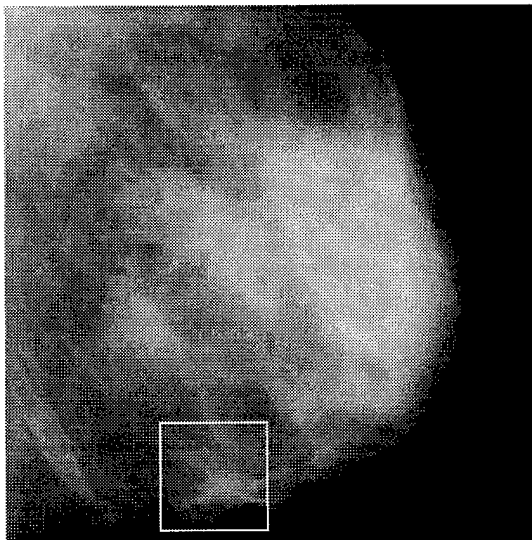


(c)

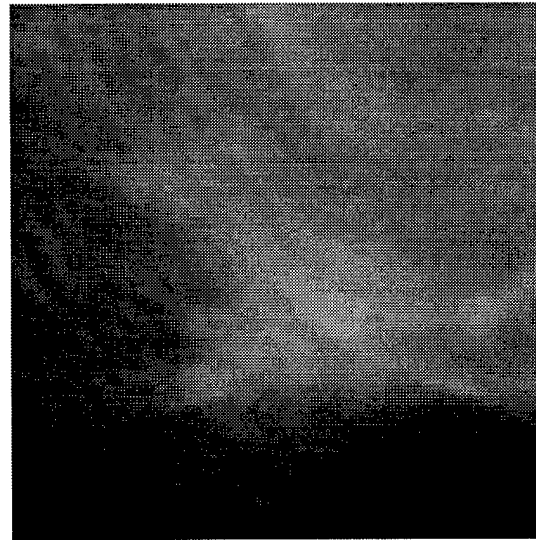


(d)

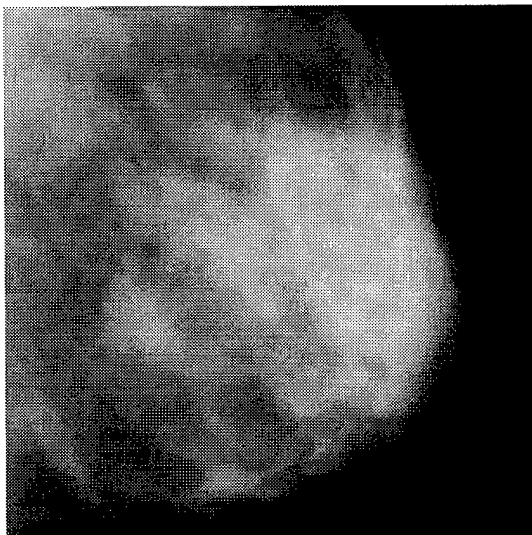
Figure 15: Image fusion of phantoms shifted by five samples. (a) Gradient pyramid. (b) Orthogonal wavelet transform. (c) Biorthogonal wavelet transform. (d) Steerable dyadic wavelet transform.



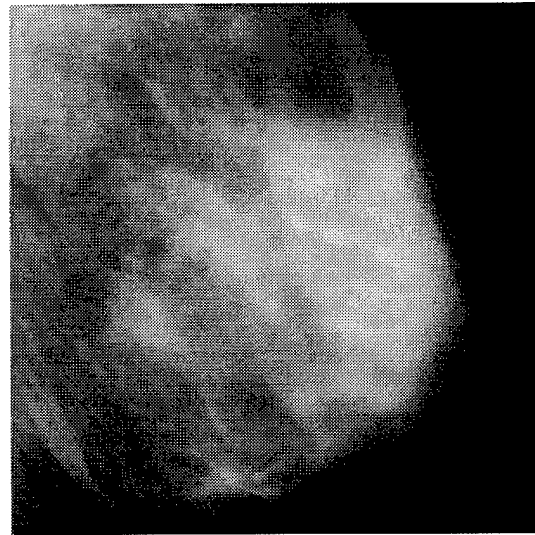
(a)



(b)



(c)

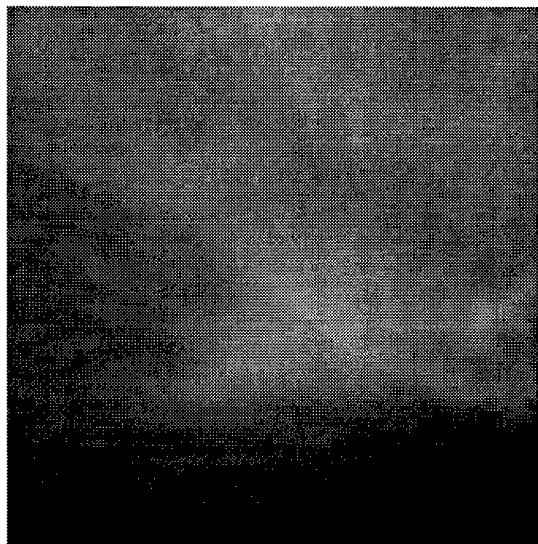


(d)

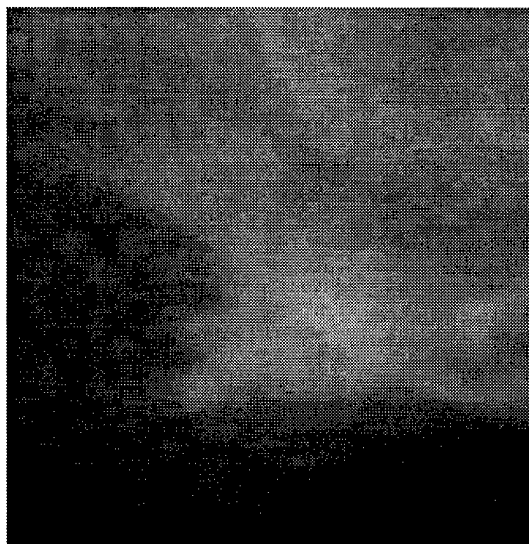
Figure 16: (a) Mammogram with area of interest delineated. (b) Area of interest. (c) Image from (a) with left half blurred. (d) Image from (a) with right half blurred.



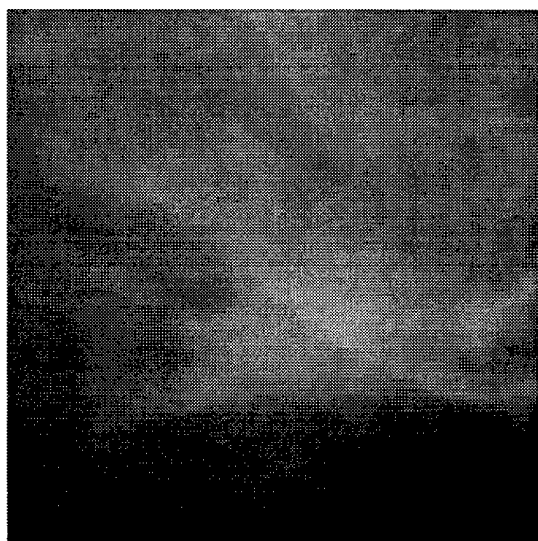
gradient pyramid, however, caused loss of sharpness.



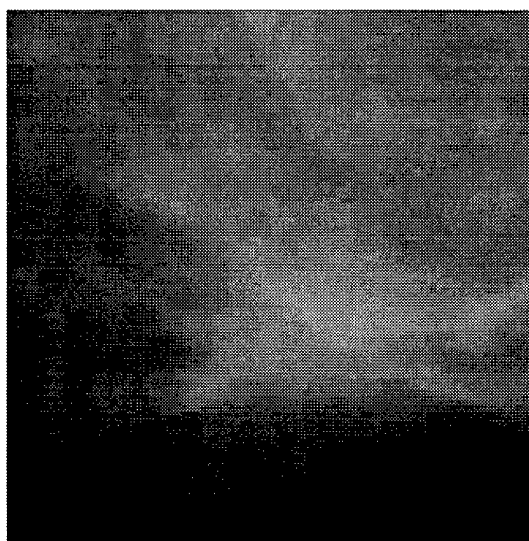
(a)



(b)



(c)



(d)

Figure 17: Region of interest corresponding to the one from Figure 16(b) extracted from the fused images using: (a) gradient pyramid, (b) orthogonal wavelet transform, (c) biorthogonal wavelet transform, and (d) steerable dyadic wavelet transform.

### 3 Conclusions

During the first year, we have made significant progress in the development of a methodology for improving the mammographic viewing environment by steerable multiscale transforms. We constructed a new transform that does not introduce artifacts due to translation and rotation invariance, which are inherent to traditional wavelet analyses, and demonstrated its usefulness for image fusion.

We extended the one-dimensional discrete dyadic wavelet transform to higher-order derivatives and even-order spline functions and developed an improved initialization procedure. Comparison to the originally employed initialization [11] showed significantly better performance of our procedure for finer scales of analysis.

We developed several two-dimensional transforms. All of them were derived with the goal of eliminating artifacts due to lack of translation and rotation invariance. We presented a two-dimensional discrete dyadic wavelet transform with a first-derivative wavelet as an extension of the one originally proposed in [11], a two-dimensional discrete dyadic wavelet transform with a second-derivative wavelet that can approximate Laplacian of a Gaussian, and a steerable dyadic wavelet transform implemented in a near-perfect reconstruction filter bank which may be preferred when there is a need for orientation processing along equally spaced angles. We derived a multiscale spline derivative-based transform which uses  $x$ - $y$  separable filters in a perfect reconstruction filter bank and enables fast translation and rotation-invariant directional analysis of images.

We compared the steerable dyadic wavelet transform with the gradient pyramid, orthogonal wavelet transform, and biorthogonal wavelet transform for fusion of features relevant to mammography. During our experiments, the steerable dyadic wavelet transform was exhibiting a combination of best properties of the gradient pyramid and of the orthogonal/biorthogonal wavelet transform. The steerable dyadic wavelet transform behaved similarly as the gradient pyramid in a sense that it did not introduce artifacts commonly present when the orthogonal and biorthogonal wavelet transforms were used. At the same time, the steerable dyadic wavelet transform outperformed the gradient pyramid by acting like the orthogonal and biorthogonal wavelet transforms in terms of mathematical criteria and sharpness in the fused image.

Our future work includes building of a unified framework for creation of a superior local mammographic viewing environment via steerable dyadic wavelet transform, and for fusion of locally obtained features for a better global mammographic viewing environment.

## References

- [1] S. L. Parker, T. Tong, S. Bolden, and P. A. Wingo, "Cancer statistics 1996," *CA-A Cancer Journal for Clinicians*, vol. 46, no. 1, pp. 5-27, 1996.
- [2] R. A. Smith, "Epidemiology of breast cancer," in *A Categorical Course in Physics, Technical Aspects of Breast Imaging*, A. G. Haus and M. J. Yaffe, Eds. The 79th Scientific Assembly and Annual Meeting of the Radiological Society of North America (RSNA), 1993, pp. 21-33.
- [3] P. C. Johns and M. J. Yaffe, "X-ray characterization of normal and neoplastic breast tissues," *Physics in Medicine and Biology*, vol. 32, no. 6, pp. 675-695, 1987.
- [4] M. J. Yaffe, R. J. Jennings, R. Fahrig, and T. R. Fewell, "X-ray spectral considerations for mammography," in *A Categorical Course in Physics, Technical Aspects of Breast Imaging*, A. G. Haus and M. J. Yaffe, Eds. The 79th Scientific Assembly and Annual Meeting of the Radiological Society of North America (RSNA), 1993, pp. 63-72.
- [5] A. F. Laine, S. Schuler, J. Fan, and W. Huda, "Mammographic feature enhancement by multiscale analysis," *IEEE Trans. Med. Imaging*, vol. 13, no. 4, pp. 725-740, 1994.
- [6] A. Laine, W. Huda, B. G. Steinbach, and J. C. Honeyman, "Mammographic image processing using wavelet processing techniques," *Eur. Radiology*, vol. 5, pp. 518-523, 1995.
- [7] A. Laine, J. Fan, and W. Yang, "Wavelets for contrast enhancement of digital mammography," *IEEE Eng. Med. Biol. Mag.*, vol. 14, no. 5, pp. 536-550, 1995.
- [8] A. Laine, J. Fan, and S. Schuler, "A framework for contrast enhancement by dyadic wavelet analysis," in *Digital Mammography*, A. G. Gale, S. M. Astley, D. R. Dance, and A. Y. Cairns, Eds., Elsevier, Amsterdam, The Netherlands, 1994, pp. 91-100.
- [9] I. Koren, A. Laine, F. Taylor, and M. Lewis, "Interactive wavelet processing and techniques applied to digital mammography," in *Proc. IEEE Int. Conf. Acoust. Speech Signal Process.*, Atlanta, GA, 1996, vol. 3, pp. 1415-1418.
- [10] J. Fan and A. Laine, "Multiscale contrast enhancement and denoising in digital radiographs," in *Wavelets in Medicine and Biology*, A. Aldroubi and M. Unser, Eds., CRC Press, Boca Raton, FL, 1996, pp. 163-189.
- [11] S. Mallat and S. Zhong, "Characterization of signals from multiscale edges," *IEEE Trans. Pattern Anal. Mach. Intell.*, vol. 14, no. 7, pp. 710-732, 1992.

- [12] I. Koren and A. Laine, "A discrete dyadic wavelet transform for multidimensional feature analysis," in *Time-Frequency and Wavelets in Biomedical Signal Engineering*, M. Akay, Ed., IEEE Press, New York, NY, 1997, pp. 425–449.
- [13] I. J. Schoenberg, "Contributions to the problem of approximation of equidistant data by analytic functions," *Q. Appl. Math.*, vol. 4, no. 1, pp. 45–99, 112–141, 1946.
- [14] I. J. Schoenberg, "Cardinal interpolation and spline functions," *J. Approx. Theory*, vol. 2, no. 2, pp. 167–206, 1969.
- [15] C. de Boor, *A Practical Guide to Splines*, Springer-Verlag, New York, NY, 1978.
- [16] M. Unser, A. Aldroubi, and M. Eden, "On the asymptotic convergence of B-spline wavelets to Gabor functions," *IEEE Trans. Inf. Theory*, vol. 38, no. 2, pp. 864–872, 1992.
- [17] I. Daubechies, *Ten Lectures on Wavelets*, SIAM, Philadelphia, PA, 1992.
- [18] C. K. Chui, *An Introduction to Wavelets*, Academic Press, San Diego, CA, 1992.
- [19] C. K. Chui, Ed., *Wavelets: A Tutorial in Theory and Applications*, Academic Press, San Diego, CA, 1992.
- [20] M. Unser, A. Aldroubi, and M. Eden, "Fast B-spline transforms for continuous image representation and interpolation," *IEEE Trans. Pattern Anal. Mach. Intell.*, vol. 13, no. 3, pp. 277–285, 1991.
- [21] A. Aldroubi, M. Unser, and M. Eden, "Cardinal spline filters: Stability and convergence to the ideal sinc interpolator," *Signal Process.*, vol. 28, no. 2, pp. 127–138, 1992.
- [22] I. J. Schoenberg, "Notes on spline functions III: On the convergence of the interpolating cardinal splines as their degree tends to infinity," *Isr. J. Math.*, vol. 16, no. 1, pp. 87–93, 1973.
- [23] A. V. Oppenheim and R. W. Schaffer, *Discrete-Time Signal Processing*, Prentice-Hall, Englewood Cliffs, NJ, 1989.
- [24] M. Unser, A. Aldroubi, and M. Eden, "Polynomial spline signal approximations: Filter design and asymptotic equivalence with Shannon's sampling theorem," *IEEE Trans. Inf. Theory*, vol. 38, no. 1, pp. 95–103, 1992.

- [25] C. E. Shannon, "Communication in the presence of noise," *Proc. IRE*, vol. 37, no. 1, pp. 10–21, 1949.
- [26] M. Unser and A. Aldroubi, "A general sampling theory for nonideal acquisition devices," *IEEE Trans. Signal Process.*, vol. 42, no. 11, pp. 2915–2925, 1994.
- [27] M. Vrhel, C. Lee, and M. Unser, "Fast computation of the continuous wavelet transform through oblique projections," in *Proc. IEEE Int. Conf. Acoust. Speech Signal Process.*, Atlanta, GA, 1996, vol. 3, pp. 1459–1462.
- [28] I. Koren, A. F. Laine, J. Fan, and F. J. Taylor, "Edge detection in echocardiographic image sequences by 3-D multiscale analysis," in *Proc. IEEE Int. Conf. Image Process.*, Austin, TX, 1994, vol. 1, pp. 288–292.
- [29] M. J. T. Smith and T. P. Barnwell, III, "Exact reconstruction techniques for tree-structured subband coders," *IEEE Trans. Acoust. Speech Signal Process.*, vol. 34, no. 3, pp. 434–441, 1986.
- [30] P. J. Burt and E. H. Adelson, "The Laplacian pyramid as a compact image code," *IEEE Trans. Commun.*, vol. 31, no. 4, pp. 532–540, 1983.
- [31] A. Witkin, "Scale space filtering," in *Proc. Int. Joint Conf. Artif. Intell.*, Karlsruhe, Germany, 1983, pp. 1019–1022.
- [32] M. Holschneider, R. Kronland-Martinet, J. Morlet, and Ph. Tchamitchian, "A real-time algorithm for signal analysis with the help of the wavelet transform," in *Wavelets, Time-Frequency Methods and Phase Space*, J. M. Combes, A. Grossmann, and Ph. Tchamitchian, Eds., Springer-Verlag, Berlin, Germany, 1989, pp. 286–297.
- [33] J. Canny, "A computational approach to edge detection," *IEEE Trans. Pattern Anal. Mach. Intell.*, vol. 8, no. 6, pp. 679–698, 1986.
- [34] W. T. Freeman and E. H. Adelson, "The design and use of steerable filters," *IEEE Trans. Pattern Anal. Mach. Intell.*, vol. 13, no. 9, pp. 891–906, 1991.
- [35] J. Babaud, A. P. Witkin, M. Baudin, and R. O. Duda, "Uniqueness of the Gaussian kernel for scale-space filtering," *IEEE Trans. Pattern Anal. Mach. Intell.*, vol. 8, no. 1, pp. 26–33, 1986.
- [36] M. Unser, A. Aldroubi, and S. J. Schiff, "Fast implementation of the continuous wavelet transform with integer scales," *IEEE Trans. Signal Process.*, vol. 42, no. 12, pp. 3519–3523, 1994.

- [37] S. Mallat and W. L. Hwang, "Singularity detection and processing with wavelets," *IEEE Trans. Inf. Theory*, vol. 38, no. 2, pp. 617–643, 1992.
- [38] A. J. Jerri, "The Shannon sampling theorem—its various extensions and applications: A tutorial review," *Proc. IEEE*, vol. 65, no. 11, pp. 1565–1596, 1977.
- [39] D. Marr and E. Hildreth, "Theory of edge detection," *Proc. R. Soc. London Ser. B*, vol. 207, no. 1167, pp. 187–217, 1980.
- [40] P. Perona, "Deformable kernels for early vision," *IEEE Trans. Pattern Anal. Mach. Intell.*, vol. 17, no. 5, pp. 488–499, 1995.
- [41] E. P. Simoncelli, W. T. Freeman, E. H. Adelson, and D. J. Heeger, "Shiftable multiscale transforms," *IEEE Trans. Inf. Theory*, vol. 38, no. 2, pp. 587–607, 1992.
- [42] Y. Hel-Or and P. C. Teo, "Canonical decomposition of steerable functions," in *Proc. IEEE Comput. Soc. Conf. Comput. Vision Pattern Recognit.*, San Francisco, CA, 1996, pp. 809–816.
- [43] H. Greenspan, S. Belongie, R. Goodman, P. Perona, S. Rakshit, and C. H. Anderson, "Overcomplete steerable pyramid filters and rotation invariance," in *Proc. IEEE Comput. Soc. Conf. Comput. Vision Pattern Recognit.*, Seattle, WA, 1994, pp. 222–228.
- [44] A. Karasarisidis and E. Simoncelli, "A filter design technique for steerable pyramid image transforms," in *Proc. IEEE Int. Conf. Acoust. Speech Signal Process.*, Atlanta, GA, 1996, vol. 4, pp. 2389–2392.
- [45] E. P. Simoncelli and W. T. Freeman, "The steerable pyramid: A flexible architecture for multi-scale derivative computation," in *Proc. IEEE Int. Conf. Image Process.*, Washington, D.C., 1995, vol. 3, pp. 444–447.
- [46] I. Koren, A. Laine, and F. Taylor, "Image fusion using steerable dyadic wavelet transform," in *Proc. IEEE Int. Conf. Image Process.*, Washington, D.C., 1995, vol. 3, pp. 232–235.
- [47] A. Laine, I. Koren, W. Yang, and F. Taylor, "A steerable dyadic wavelet transform and interval wavelets for enhancement of digital mammography," in *Wavelet Applications II*, Proc. SPIE, H. H. Szu, Ed., Orlando, FL, 1995, vol. 2491, pp. 736–749.
- [48] O. Rioul and P. Duhamel, "Fast algorithms for discrete and continuous wavelet transforms," *IEEE Trans. Inf. Theory*, vol. 38, no. 2, pp. 569–586, 1992.

- [49] P. J. Burt and R. J. Kolczynski, "Enhanced image capture through fusion," in *Proc. Int. Conf. Comput. Vision*, Berlin, Germany, 1993, pp. 173–182.
- [50] A. Toet, "Image fusion by a ratio of low-pass pyramid," *Pattern Recognit. Lett.*, vol. 9, no. 4, pp. 245–253, 1989.
- [51] L. J. Chipman, T. M. Orr, and L. N. Graham, "Wavelets and image fusion," in *Proc. IEEE Int. Conf. Image Process.*, Washington, D.C., 1995, vol. 3, pp. 248–251.
- [52] H. Li, B. S. Manjunath, and S. K. Mitra, "Multi-sensor image fusion using the wavelet transform," in *Proc. IEEE Int. Conf. Image Process.*, Austin, TX, 1994, vol. 1, pp. 51–55.
- [53] T. Ranchin, L. Wald, and M. Mangolini, "Efficient data fusion using wavelet transform: the case of SPOT satellite images," in *Mathematical Imaging: Wavelet Applications in Signal and Image Processing*, Proc. SPIE, A. F. Laine, Ed., San Diego, CA, 1993, vol. 2034, pp. 171–178.
- [54] S. G. Mallat, "A theory for multiresolution signal decomposition: the wavelet representation," *IEEE Trans. Pattern Anal. Mach. Intell.*, vol. 11, no. 7, pp. 674–693, 1989.